SCIENTIFIC REPORTS

OPEN

SUBJECT AREAS:
SOLID EARTH SCIENCES
GEODYNAMICS
BIOGEOCHEMISTRY
VOLCANOLOGY

Received
26 February 2013

Accepted
23 July 2013

Published
13 August 2013

Correspondence and requests for materials should be addressed to S.P.K. (kilias@geol.uoa.gr)

New insights into hydrothermal vent processes in the unique shallow-submarine arc-volcano, Kolumbo (Santorini), Greece

Stephanos P. Kilias[1], Paraskevi Nomikou[1], Dimitrios Papanikolaou[1], Paraskevi N. Polymenakou[2], Athanasios Godelitsas[1], Ariadne Argyraki[1], Steven Carey[3], Platon Gamaletsos[1,6], Theo J. Mertzimekis[4], Eleni Stathopoulou[5], Joerg Goettlicher[6], Ralph Steininger[6], Konstantina Betzelou[1], Isidoros Livanos[1], Christos Christakis[1,2], Katherine Croff Bell[3] & Michael Scoullos[5]

[1]National and Kapodistrian University of Athens, Faculty of Geology and Geoenvironment, Panepistimiopoli Zografou, 15784 Athens, Greece, [2]Hellenic Centre for Marine Research, Institute of Marine Biology, Biotechnology and Aquaculture, Gournes Pediados, P.O.Box 2214, Gr 71003, Heraklion Crete, Greece, [3]Graduate School of Oceanography, University of Rhode Island, 215 S. Ferry Road, Narragansett, Rhode Island 02882, USA, [4]National and Kapodistrian University of Athens, Faculty of Physics, Panepistimiopoli Zografou, 15784 Athens, Greece, [5]National and Kapodistrian University of Athens, Faculty of Chemistry, Panepistimiopoli Zografou, 15784 Athens, Greece, [6]Karlsruhe Institute of Technology, ANKA Synchrotron Radiation Facility, Hermann-von-Helmholtz-Platz 1, 76344 Eggenstein-Leopoldshafen, Germany.

We report on integrated geomorphological, mineralogical, geochemical and biological investigations of the hydrothermal vent field located on the floor of the density-stratified acidic (pH ~ 5) crater of the Kolumbo shallow-submarine arc-volcano, near Santorini. Kolumbo features rare geodynamic setting at convergent boundaries, where arc-volcanism and seafloor hydrothermal activity are occurring in thinned continental crust. Special focus is given to unique enrichments of polymetallic spires in Sb and Tl (±Hg, As, Au, Ag, Zn) indicating a new hybrid seafloor analogue of epithermal-to-volcanic-hosted-massive-sulphide deposits. Iron microbial-mat analyses reveal dominating ferrihydrite-type phases, and high-proportion of microbial sequences akin to *"Nitrosopumilus maritimus"*, a mesophilic Thaumarchaeota strain capable of chemoautotrophic growth on hydrothermal ammonia and CO_2. Our findings highlight that acidic shallow-submarine hydrothermal vents nourish marine ecosystems in which nitrifying Archaea are important and suggest ferrihydrite-type Fe^{3+}-(hydrated)-oxyhydroxides in associated low-temperature iron mats are formed by anaerobic Fe^{2+}-oxidation, dependent on microbially produced nitrate.

Most hydrothermal vent studies have dealt with mid-ocean ridges (Fig. 1a), intraoceanic island arcs (e.g. Philippines) (Fig. 1b) or subduction systems beneath active continental margins with back-arc marginal basins (e.g. Japan) (Fig. 1c). However, unique but less studied, transitional situations exist in convergent settings such as in the Hellenic Volcanic Arc (HVA), where volcanism and hydrothermal activity occur through thinned continental crust. The HVA is a young 5 Ma-to-present volcanic arc that has developed in the pre-Alpine to Quaternary continental crust of the Hellenic Subduction System (HSS)[1,2]. Its development is a response to the northward subduction of the last remnant of the oceanic crust of the African plate beneath the southern edge of the active margin of the European plate[3].

The HSS is a special situation not conformable to the usual geodynamic setting known from Pacific convergent settings[4]. The basic difference is that HVA (Methana, Milos, Santorini, Nisyros) is separated from the Hellenic Sedimentary Arc (HSA) (Peloponnesus, Crete, Rhodes) by the Cretan basin, a "back-arc" mollasic basin which lies behind the HSA but in front of the HVA (Fig. 1d).

The Cretan Basin is the result of extension north of Crete, whereas the Hellenic trench and fore arc basin of the HSS south of Crete is dominated by compression[3]. Kolumbo has evolved within a local transtensional tectonic regime of the overall compressive regime of the HSS[3]. It is a small submarine volcano of the HVA, located in the Aegean Sea about 7 km off the north-eastern coast of Santorini, Aegean Sea, along a northeast-southwest-trending

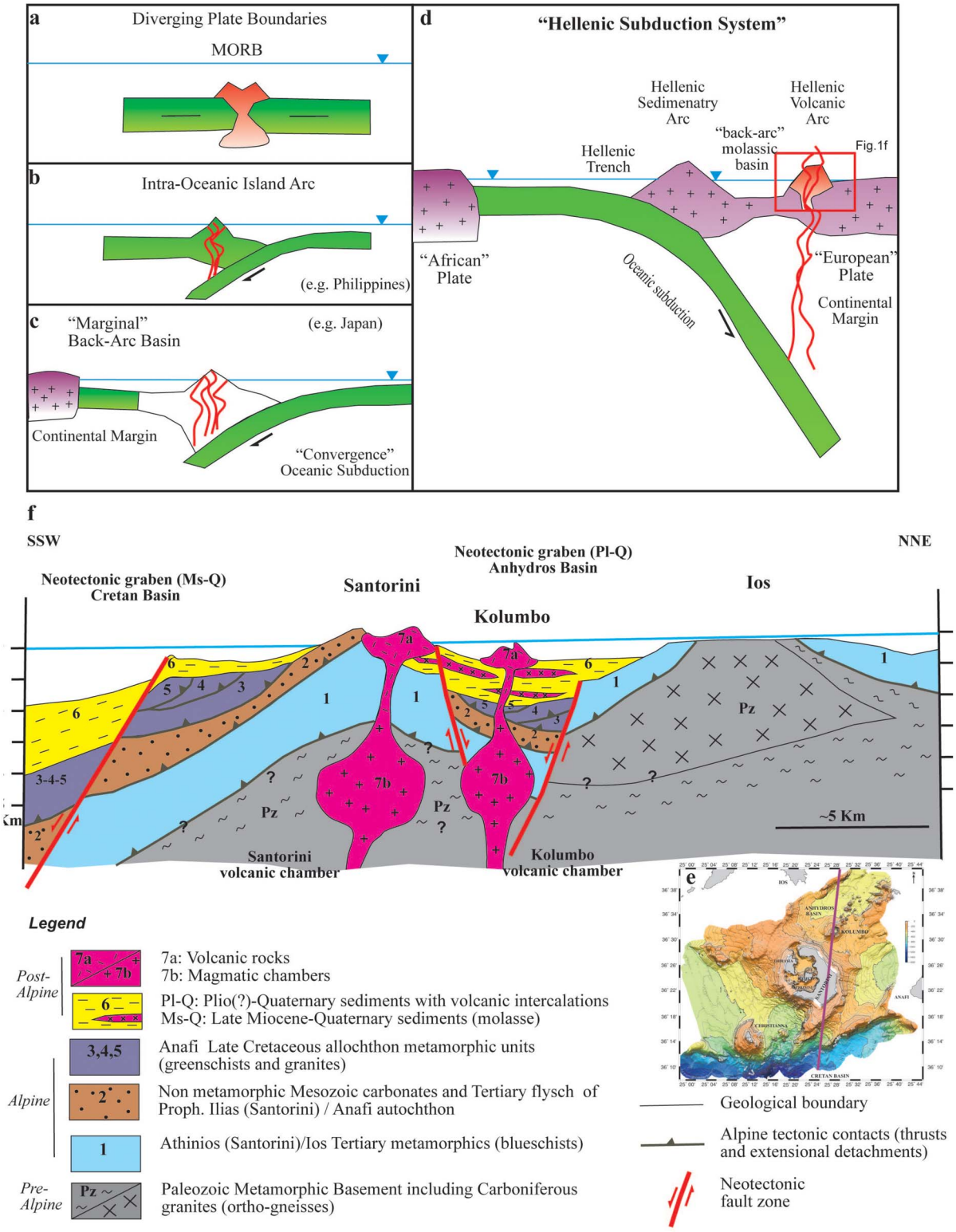

Figure 1 | Tectonic setting of the Santorini-Kolumbo volcanic field. (a–d): Schematic cartoons of different geodynamic environments where seafloor hydrothermal vents occur. (a) Mid-Ocean Ridges along divergent plates. (b) Intra-Oceanic Arcs within convergent boundaries (e.g. Philippines). (c) Marginal back-arc basins and island arcs along active continental margins with oceanic subduction (e.g. Japan). (d) "Hellenic Subduction System". The "Hellenic Volcanic Arc", within active continental margin, developed behind the molassic back-arc basin, hosted over thinned continental crust. (e) Swath bathymetry map of Santorini-Kolumbo volcanic field (modified after ref. 5-permission to publish the original map was provided by Elsevier Science) and location of the geological transect (red line). (f) Schematic cartoon depicting the geological cross section through the Hellenic Volcanic Arc, from the molassic back-arc Cretan Basin to the Cycladic island of Ios in the back-arc area.

linear volcano-tectonic field that extends for some 20 km (Fig. 1e)[5]. Kolumbo, which is the largest cone of this submarine field, erupted explosively in 1650 AD causing about 70 fatalities on Santorini from toxic gases[5].

Submarine hydrothermal vents are well known for hosting unique, highly productive chemoautotrophic microbial communities[6]. Microrganisms are involved at various levels in the transformation of rocks and minerals at and below the seafloor, therefore microbe-minerals interactions in hydrothermal vents are thought to play an important role in global biogeochemical element cycles, and biomineralization[6,7].

This paper's objective is to characterize for the first time the Kolumbo hydrothermal vent system, using a multidisciplinary approach including geomorphological, mineralogical, geochemical and biological research data.

Results

Geological and morphological setting. Kolumbo is built on pre-Alpine continental basement of the Cyclades (10-15 km thick) consisting of a core of Carboniferous granites (ortho-gneisses) and a sequence of garnet-mica schists corresponding to the Palaeozoic Metamorphic Basement cropping out on Ios Island[8]. Alpine blueschists and overlying nappes comprising both metamorphosed in Late Cretaceous, greenschists, marbles, metaophiolites and metagranites and unmetamorpshosed Mesozoic, carbonates and Tertiary flysch, are found respectively on top of the pre-Alpine Basement (Fig. 1f). Kolumbo volcano and the other 19 submarine cones[5,9] are lying within the Plio-Quaternary marine sediments of the extensional Anhydros basin bordered by marginal fault zones. This linear contribution of the volcanic cones is controlled by the NE-SW Christiana-Santorini-Kolumbo (CSK) volcano-tectonic zone which provides pathways for subduction-generated magmas to reach the surface[9] (Fig. 1f).

Kolumbo's elongated cone has a basal diameter of 7 km, a crater width of 1.7 km and rises up from a water depth of at least 504 m to 18 m (ref. 10) (Fig. 2a). The crater walls expose stratified pumiceous deposits at a depth of 270-250 m which continue to 150 m, above which the deposits are obscured by loose talus and bacterial overgrowths[10]. Analyzed pumice from Kolumbo crater walls, is largely high-K rhyolite (73.7 to 74.2 wt% SiO_2 and 3.85 to 3.94 K_2O; 4 analyses) with a high pre-eruption volatile content of 6–7% (ref. 11). The eastern crater walls depict some massive lava flows with impressive columnar jointing and isolated NE-SW trending dikes parallel to the CSK[9,11]. In 2006, Remotely Operated Vehicle explorations in the northern part of Kolumbo's crater floor revealed an extensive "diffuse-flow"-style hydrothermal vent field, Kolumbo Hydrothermal Field (KHF)[12], between 492 and 504 m depth. In 2010 and 2011, onboard E/V Nautilus, a bathymetric map of KHF was created (Fig. 2b) by utilizing the 1,375 kHz BlueView multibeam sonar, structured light and stereo imagery data[13] acquired by the ROV Hercules. The detailed swath bathymetric mapping using 0.5 m grid interval revealed an extensive field with numerous active vents in the central part of KHF, with larger but less active vents occurring in the northern part of the crater floor.

Hydrothermal vents. Virtually the entire crater floor of Kolumbo (area of approximately 600 × 1200 m) is covered by a few-cm-thick orange to brown smooth sediment[10] that consists of Fe-encrusted flocculent microbial mats and amorphous Fe-oxyhydroxide deposits. Temperature in the Fe-rich sediment varies between 16.2°C and 17°C. Clear, low-temperature fluids (≤70°C) and CO_2 gas bubbles slowly discharge from the Fe microbial mats through small pockmark–like craters (Supplementary Fig. S1). This "diffuse-flow" may be supporting microbiological productivity on Kolumbo's crater floor and may be linked to Fe-mat formation[14]. The seawater column in the crater at depths >250 m, is strongly clouded with reddish-orange and white particles, most likely of Fe-rich plume-dispersed flocculent pieces of the microbial mat. Towards the base of the northern wall at depths of ~490 m, white microbial mats were observed as streaks on the wall, interpreted as the result of colonization of low-temperature probably dense-fluid seeps.

The KHF consists dominantly of active and inactive sulphide-sulphate structures in the form of vertical spires and pinnacles, mounds and flanges along a NE-SW trend, sub-parallel to the CSK volcano-tectonic zone[9]. These vents are surrounded by sites of low-temperature (≤70°C) diffuse venting from the Fe-mats. A typical spire-type vent, named Politeia Vent Complex ("Politeia"), covers an area of 5 × 5 m (Supplementary Fig. S1) in the western part of the KHF. It is dominated by short (≤3 m tall), slender, intermediate-temperature diffusely-venting, isolated and/or merged, sulphide-sulphate spires or "diffusers"[15,16] (Supplementary Fig. S1). These spires usually taper to their top, and rise up from a hydrothermal mound that grows directly on the sediment and Fe mat-covered seafloor. "Diffuser" spires at Kolumbo discharge clear shimmering fluids, from which sulphide minerals have precipitated prior to discharge[17]. Similar vents have been observed at shallow-water boiling vents on the Tonga arc, SW Pacific[18] and the Mid-Atlantic Ridge near Iceland[19]. The spires lack beehive structures, "black smoke", and an axial conduit that typify "black smoker" chimneys[15,16]. The exterior of the Politeia spires is covered by grayish suspended filamentous microbial biofilms (streamers) that could not be recovered (Supplementary Fig. S1).

In the central part of the vent field are smooth-sided sulphide-sulphate mounds such as the Champagne Vent Complex ("Champagne") and the "Diffuser II Vent Complex ("Diffuser II") (Supplementary Fig. S1) that are covered by orange to brown Fe-rich microbial mats. They consist of a basal mound with no spire structures, and commonly discharge streams of bubbles, mainly CO_2, from small holes and cracks on their sides and bases; dissolution of the gas causes accumulation of stably-stratified CO_2-rich water within the enclosed basin of the Kolumbo crater, and the accumulation of acidic seawater above the vents[20] (as low as pH 5.0). In the absence of dissolved oxygen data, a hypothesis of oxygen depletion near the crater floor can be based on the CO_2-induced density stratification within the crater[20]. This phenomenon probably leads not only to accumulation of acidic water that is impeded from vertical mixing, but also to oxygen deprivation by precluding efficient transfer into the deeper layer of the oxygenated surface seawater. The highest vent temperature that was measured in 2010 was 210°C. The largest observed hydrothermal vent with Fe microbial mat covering is Poet's Candle (height ~ 4 m), located at the northern crater slope with no clear evidence of shimmering fluids (Supplementary Fig. S1).

Two massive sulphide-rich spires, Politeia spire-1 and Politeia spire-2 (sample NA014-003 and NA014-039 in Table 1, respectively), were recovered from "Politeia" (Supplementary Fig. 1) at ~500 m depth. The spires were intact and measured ~25 cm long and ~15 cm in diameter (Supplementary Fig. S1). They consist of an anastomozing, discontinuous array of narrow (≤2 cm diameter) channels delineating original fluid-flow paths, occurring within a porous sponge-like spire interior. Four mound samples with variable amounts of sulphide and sulphate were collected from vents actively discharging gaseous CO_2 (>99 weight%); three from "Champagne" (samples NA014-007, NA014-027 and NA014-028), and one from "Diffuser II" (sample NA014-005).

A vertical water sampling profile (Fig. 3) conducted directly above the active "Champagne" vent, showed significant positive correlation between the distribution of NH_4^+ and filterable (< 0.45 μm) Fe_{FT} ($R = 0.97, p < 0.008$ Pearson). The highest levels of NH_4^+ (21 μmol L^{-1}) and Fe_{FT} (2.1 μmol L^{-1}) were recorded at 500 m depth just above the active vent, while an abrupt decrease in their concentration (14 and 44 fold respectively) was observed within the zone 500 to 400 m depth. These two profiles are almost mirror images of the pH distribution indicating injection of significant hydrothermal quantities of

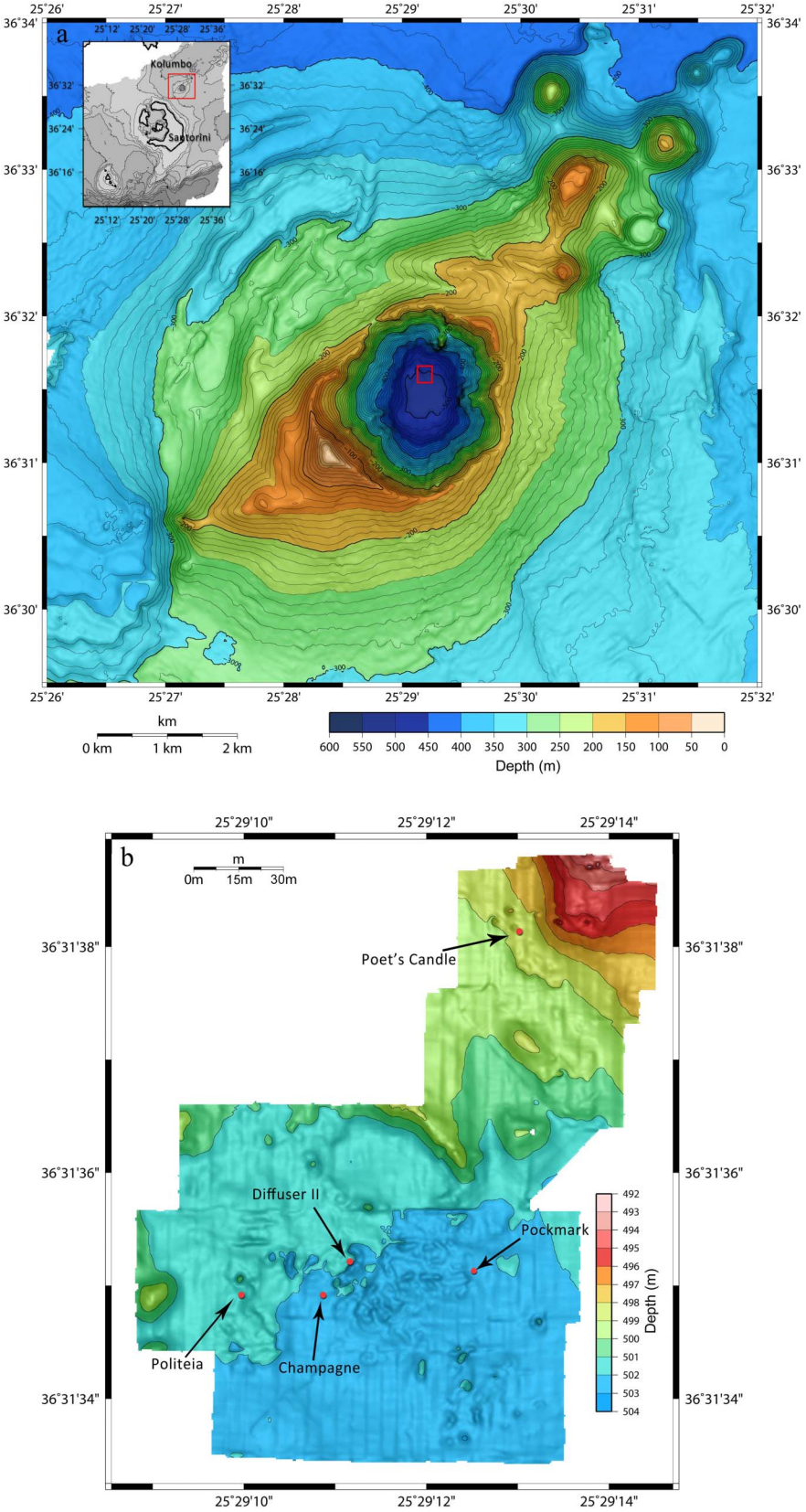

Figure 2 | Bathymetric maps for Kolumbo Volcano and hydrothermal vents. (a) Swath bathymetry of Kolumbo volcano (modified after ref. 5- permission to publish the original map was provided by Elsevier Science). (b) Detailed bathymetric map of Kolumbo hydrothermal vent field located in the northern part of the crater floor (red square in a). The location of hydrothermal vents, Politeia, Champagne, Diffuser II and Poet's Candle are indicated by red dots. Most active vents are located in the southern part of the field and larger, less active vents in the northern part. Raw data were processed by MBSystem and GMT software.

Table 1 | Average content in ppm (mg kg^{-1}) of selected elements in hydrothermal vent samples from the Kolumbo deposit

Sample	Si	Al	Fe	Pb	As	Sb	Zn	Cu	Hg	Tl	Ag	Au
NA014-003 Politeia spire-1 (ISSC)	11000	3070	107000	>10000	2740	>2000	>10000	1210	>100	435	>100	17
NA014-003 Politeia spire-1 (OAsL)	36400	688	6850	5930	>10000	>2000	5950	35	>100	>1000	>100	0.9
NA014-003 Politeia spire-1 (SFeC)	21100	1010	19800	4130	7290	>2000	1470	11	>100	868	>100	0.7
NA014-003 Politeia spire-1 composite	14100	9280	163000	66400	6430	12600	60900	1690	571	505	1710	18
NA014-005 Diffuser II		7470	311000	42500	5440	4650	1210	2760	0.1	50	763	16
NA014-007 Champagne active mound (base)	16600	16500	313000	19700	2290	8010	3900	848	967	260	218	2
NA014-016 Poet's Candle sulphide		5910	172000	53500	2640	5680	17800	2210	1	200	686	9
NA014-027 Champagne active mound-1 (N = 2)	25100	3240	242000	28800	2910	5690	2630	1510	1074	429	191	6
NA014-028 Champagne active mound -2 (N = 2)	11700	1170	217000	55700	5770	6300	3620	3480	0.7	831	614	5
NA014-039 Politeia spire-2 (ISSC)	9070	4920	201000	>10000	2230	>2000	>10000	2940	>100	415	>100	32
NA014-039 Politeia spire-2 (SFeC)	5280	1270	10600	5990	747	1380	1430	10	79	80	>100	0.4
NA014-039 Politeia spire-2 composite	2510	5470	101000	67100	2350	22400	3060	1300	481	280	1910	12
AVERAGE	14100	5890	166000	35000	3810	8330	10200	1640	397	389	871	9
MAX	36400	16500	313000	67100	7290	22400	60900	3761	1070	868	1910	32
N	12	14	14	10	13	8	10	14	8	13	7	14

both species from the seafloor into the water column (see Figure 3). Intercomparison of the profiles of the nitrogenous species indicate an upward gradual oxidation of NH_4^+ to NO_2^- and finally to NO_3^- reaching 30 μmol L^{-1} at the 200 m depth, just below the euphotic zone. Such concentrations are by far higher than the "typical" for the region undeniable proving the NH_4^+ emanating from the seafloor vents (nutrients' concentration range in seawater profiles from the Santorini Caldera is 57–276 nmol L^{-1} NH_4^+ , 21–87 nmol L^{-1} NO_2^-, 45–1,500 nmol L^{-1} NO_3^- while for Fe it is 13–115 nmol L^{-1}). The aforementioned oxidation of NH_4^+ is followed by pH increase indicating CO_2 depletion.

Characterization of solid hydrothermal phases and Fe mat deposits. Optical microscopy, powder X-ray diffractometry (PXRD) and Scanning Electron Microscopy-Energy Dispersive Spectrometry (SEM-EDS) have revealed that the bulk of the Politeia spire-1 and spire-2 structures consist of a lithified dark-gray inner sulphide-sulphate core (ISSC), 4 cm across near the top and 15 cm across at the base (Fig. 4a and Supplementary Fig. S1). The ISSC is mantled by a thin outer rind composed of a colourful "outer As-sulphide layer" (OAsL) (1-3 cm wide) which in turn is covered by a gelatinous orange to brown Fe microbial mat designated as "surface Fe-rich crust" (SFeC) (Fig. 4a and Supplementary Fig. S1).

The major PXRD-crystalline phase comprising the ISSC is barite ($BaSO_4$) together with galena (PbS), sphalerite (ZnS) and pyrite (FeS_2). According to SEM-EDS, disseminated pyrite textures include small concentric spheres, and intricate colloform-banded masses, commonly intergrown with complex Sb-Pb-sulfosalts, and non-isopachous microstromatolite-like wavy bands (Fig. 4b). Elemental mapping of these textures revealed strong chemical banding in the pyrite composition with some bands enriched in Sb (up to 19 wt%), and Pb (up to 30.3 wt%), as well as lesser amounts of As (up to 0.9 wt%). Barite is typically forming rosettes and plumose aggregates (Fig. 4b and Supplementary Fig. S2).

According to PXRD, the OAsL and SFeC samples are mineralogically identical, composed chiefly of crystalline barite and gypsum. However, the bulk of OAsL consists of PXRD-amorphous disseminated As-rich sulphides with typical colors of, and compositions approximating, orpiment (As_2S_3) and realgar (AsS), within a barite and gypsum matrix (Fig. 4c), and it is overgrown by an orange to brown mat (SFeC) dominated by PXRD-amorphous Fe-(hydrated)-oxyhydroxides (Fig. 4d and Supplementary Fig. S1). The interior porous conduits are lined by barite and gypsum overgrown by dark violet metallic aggregates of unidentified PXRD-amorphous Sb-Zn-S phases (Fig. 4e); the latter are locally overgrown by PXRD-amorphous K-Mg-Al-silicate, and/or Al-K-Fe-sulphate phases (see

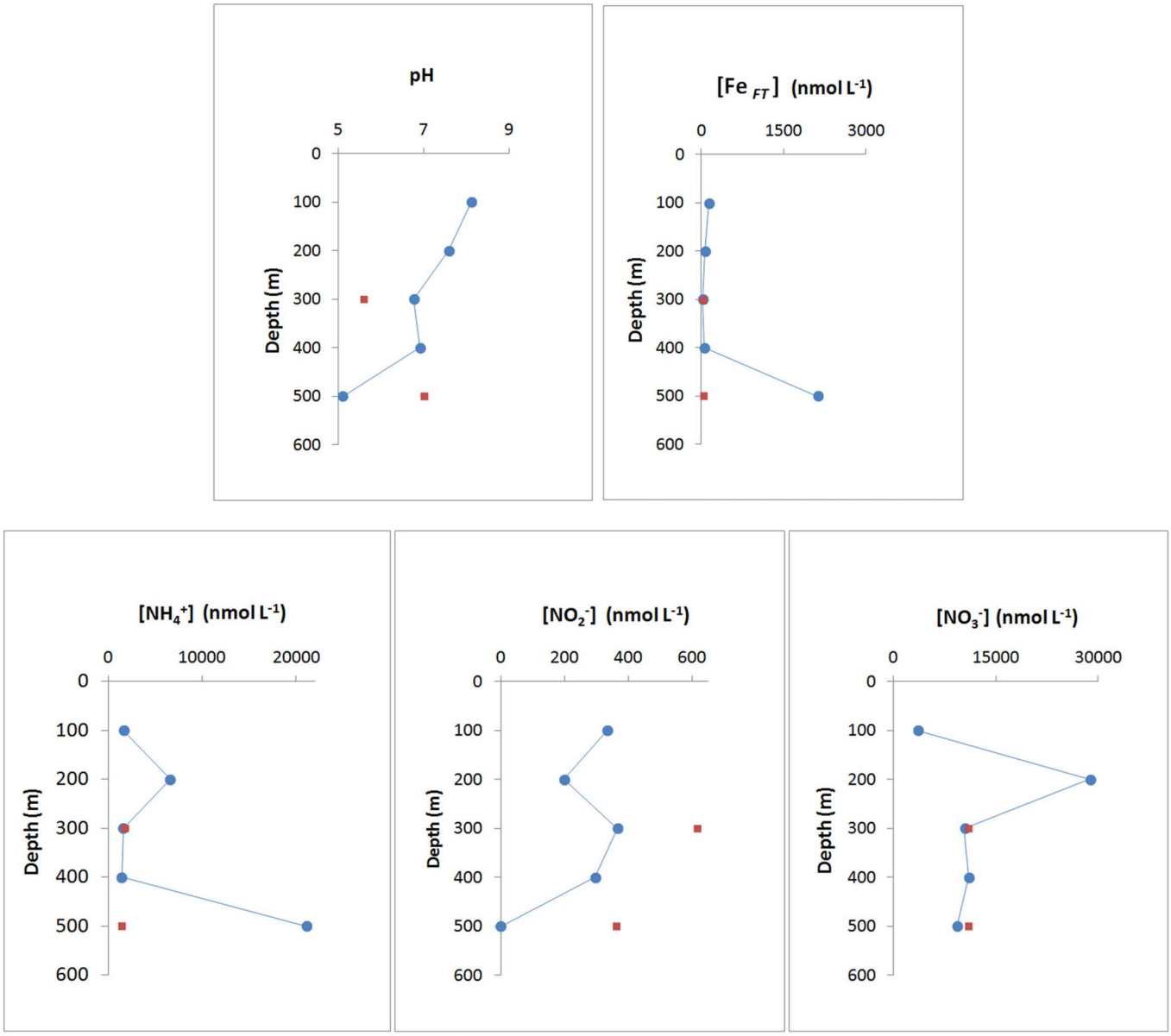

Figure 3 | Distribution of pH, Fe_{FT} and N species in the sea water column directly above Champagne vent. Depth profiles (100–500 m) indicate injection of hydrothermal NH_4^+ and iron from the seafloor to the water column and biological mediated NH_4^+ oxidation below the euphotic zone. Square symbols denote background measurements at the south side of Kolumbo crater, an area without apparent active venting.

Supplementary Fig. S3). The microscale morphologies of Fe-(hydrated)-oxyhydroxides, As-sulphides, and Sb-Zn-S phases, are dominated by delicate structures similar to microbial-like structures such as straight or branching filaments to composite filament networks, straight sticks, rods, cocci and spheres, and their aggregates, occasionally embedded in, or coated by, a smooth gel-like material, resembling fossil extracellular polymeric substances[21] (Fig. 4c,d,e). Some structures are remarkably similar to biogenic Fe oxyhydroxide-encrusted microbial structures described from hydrothermal vents of the Juan de Fuca Ridge[22,23], and the Loihi seamount[14]. Mineralized microbe structures described from Edmond vent field[24], the Lau Basin hydrothermal field[25], and the Giggenbach submarine volcano[26], are also commonly found in the "Politeia" samples.

To confirm the chemical and to determine the structural character of the Fe- and As-precipitates a Synchrotron-based spectroscopic investigation was performed on the OAsL and SFeC material. In Figure 5a the normalized Fe *K*-edge XANES spectrum recorded from the SFeC material is compared to selected reference iron spectra. The XANES spectra revealed that SFeC sample contained iron in the +3 oxidation state[27]. The experimental Fe *K*-edge EXAFS for the SFeC material was compared to respective spectra of iron reference materials, including ferrihydrite ($Fe_{10}O_{14}(OH)_2.\chi H_2O$) and goethite (FeOOH) (Fig. 5b,c). The SFeC Fe EXAFS signal is similar to that of ferrihydrite, strongly suggesting significant structural similarity between Fe-(hydrated)-oxyhydroxides in SFeC and the ferrihydrite reference materials. This is also supported by comparing the corresponding Fourier transformed (FT) magnitudes of Fe EXAFS spectra of SFeC, with those of goethite and ferrihydrite shown in Figure 5d. The Fe-Fe configuration of SFeC, represented by two second shell FT peaks, matches better with the second shell peaks of ferrihydrite than of goethite (Fig. 5d).

The normalized As *K*-edge XANES spectrum of OAsL compared with that of the reference materials, shows that the oxidation state of As in the material varies between -1 and +3 (Fig. 5e). The best match is with the XANES spectrum of As_2S_3 (orpiment). Also, Fourier transform (FT) EXAFS As *K*-edge spectrum of the OAsL material

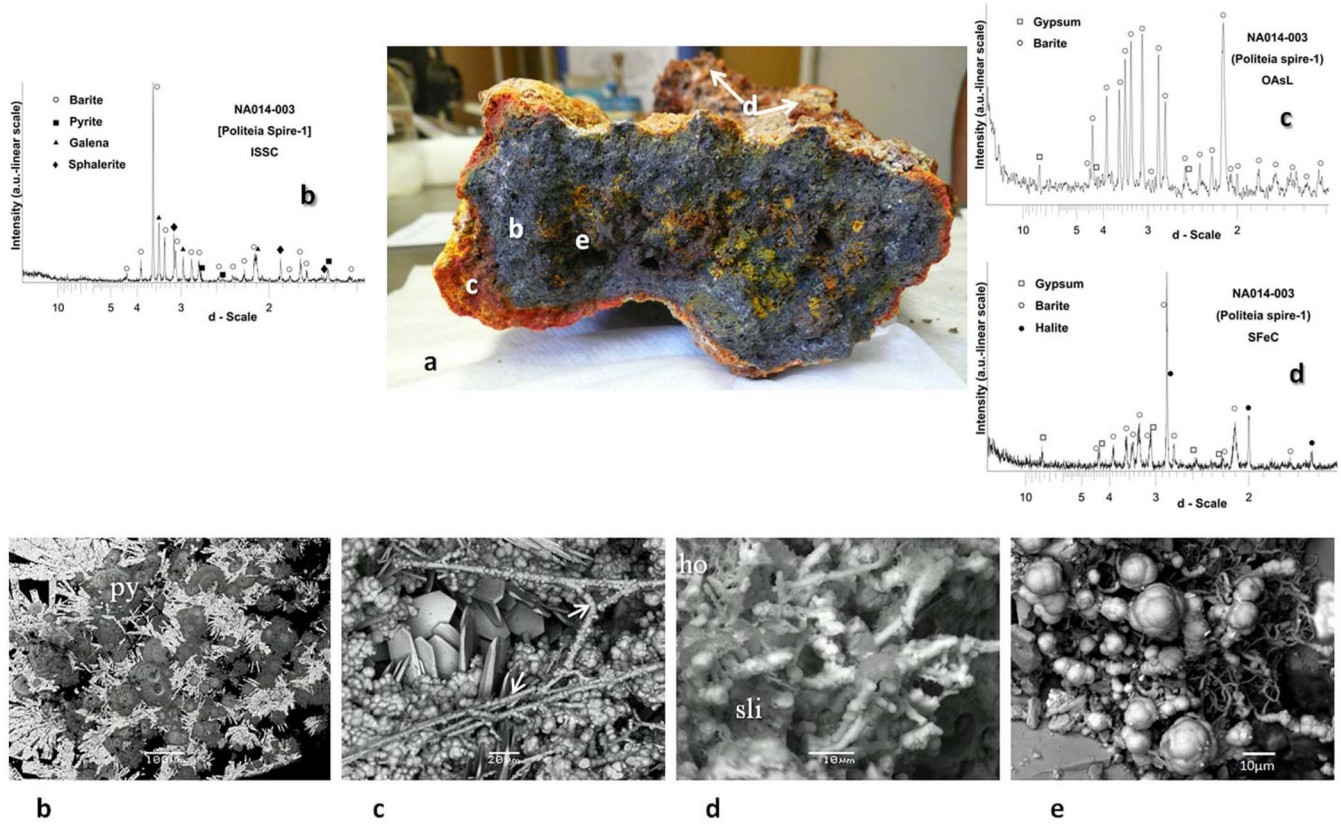

Figure 4 | Sampled spire from Politeia Vent Complex and SEM-BSE micrographs of hydrothermal precipitates with fragile morphologies (sample NA014-003). *Upper part*: (a) Basal cross section of sulphide-sulphate spire showing a thick porous ''inner sulphide-sulphate core'' (ISSC) (b) (surrounded by an earthy thin orange-yellow outer As-sulphide-dominated layer (OAsL) (c) that grades into an orange to brown Fe-(hydrated)-oxyhydroxide-dominated microbial surface Fe crust (SFeC) (d). Unidentified dark-violet phases similar to Sb-Zn-S phases are lining interior porous conduit network (e). PXRD patterns for b, c, and d are also shown. *Bottom part:* (b) SEM image of barite laths and rosettes forming a substrate for disseminated sulphides of mainly colloform banded pyrite (py). (c) Overview of amorphous orpiment (As_2S_3)-type (characterized by XAFS) phase morphologies, including clustered microspheres and globular aggregates of various sizes(1-10 µm), and straight, curved and branching filaments with ringed grooves (white arrows), overlying layer of barite blades. (d) Amorphous ferrihydrite-type (characterized by XAFS) Fe-(hydrated) -oxyhydroxides occurring as laterally extensive slime-like material (sli), locally perforated by holes (ho), forming an intimate extension of straight and/or curved filamentous, coccoidal, rod-shaped, and long straight stick structures. (e) Overview of Sb-Zn-S phase morphologies including curved and twisted hair-like filaments entwined with each other forming dense arrays and colonizing barite crystal face (ba). A large variation in additional accumulation of oblate or imperfect aggregated microspheres developed on the surface of filaments can been seen.

demonstrates structural similarities with the orpiment (As_2S_3) reference material (Fig. 5f). The first shell corresponds to sulfur atom, as first neighbor of the As central atom, reflecting the As-S interatomic distance and coordination. Additionally, the best fit of the first shell of OAsL and orpiment RDFs indicates that the OAsL structure reflects an orpiment-type structure[28]. The external surface of the ''Champagne'' vent contains botryoidal aggregates of pyrite and/or marcasite associated with euhedral gypsum and barite, and local aggregates of twinned chalcopyrite ($CuFeS_2$) crystals (see Supplementary Fig. S2).

Elemental enrichment of vent samples. Mineralized samples from the ''Politeia'' and ''Champagne'' vent complexes were analyzed for their major and trace elements (Table 1 and Supplementary Table S1). Sulfur, Fe, Ba, Si, Pb, Zn, Sr are the major elements in the samples occurring mainly as crystalline pyrite, barite, galena and sphalerite, as well as K-Mg-Al-silicate, and/or Al-K-Fe-sulphate, phases. Average basemetal concentrations for all mineralized samples are 1.0 wt percent Zn (max: 6 wt%, n = 10), 0.16 wt percent Cu (max: 0. 37 wt%, n = 14), and 3.4 wt percent Pb (max: 6.7 wt%, n = 10). Combined Zn + Cu + Pb for these samples is on average less than 4.5 wt%, which is lower compared to most seafloor sulphide deposits[17] (Supplementary Table S2). These low concentrations, especially Cu (≤0.37 wt%) probably indicate relatively low vent fluid temperatures at Kolumbo. Furthermore, trace elements usually associated with high-temperature hydrothermal activity, such as Co, Se, and Mo, are below their detection limit. Compared with data from other silicic arc-related deposits the average concentrations of Fe (16.6 wt%) in Kolumbo sulphide-sulphate-rich samples are similar, reflecting the abundance of pyrite in most samples. However, samples from Kolumbo are depleted in Si (avg.: 1.4 wt%, max: 3.6 wt%, n = 12) and Al (avg: 0.6 wt%, max: 1.6 wt%, n = 14) (Table 1), reflecting the notable lack of silica (SiO_2).

The average and maximum concentrations of Tl (510 mg kg^{-1} and >1,000 mg kg^{-1} respectively) and Sb (8,330 mg kg^{-1} and 2.2 wt%, respectively) are among the highest reported from modern seafloor hydrothermal systems. Maximum Tl concentrations were measured in Fe- and As-rich samples of Politeia's spire-1 rind, and are unique among seafloor hydrothermal deposits (Supplementary Fig. S4, and Supplementary Table S1). Moreover, the average Hg concentration is also higher than all reported values from other seafloor vents with the exception of Palinuro volcano in the Tyrrhenian Sea (Supplementary Table S1). No Tl- and Hg-bearing minerals have been detected, however, the association of Hg with Al (similarity level

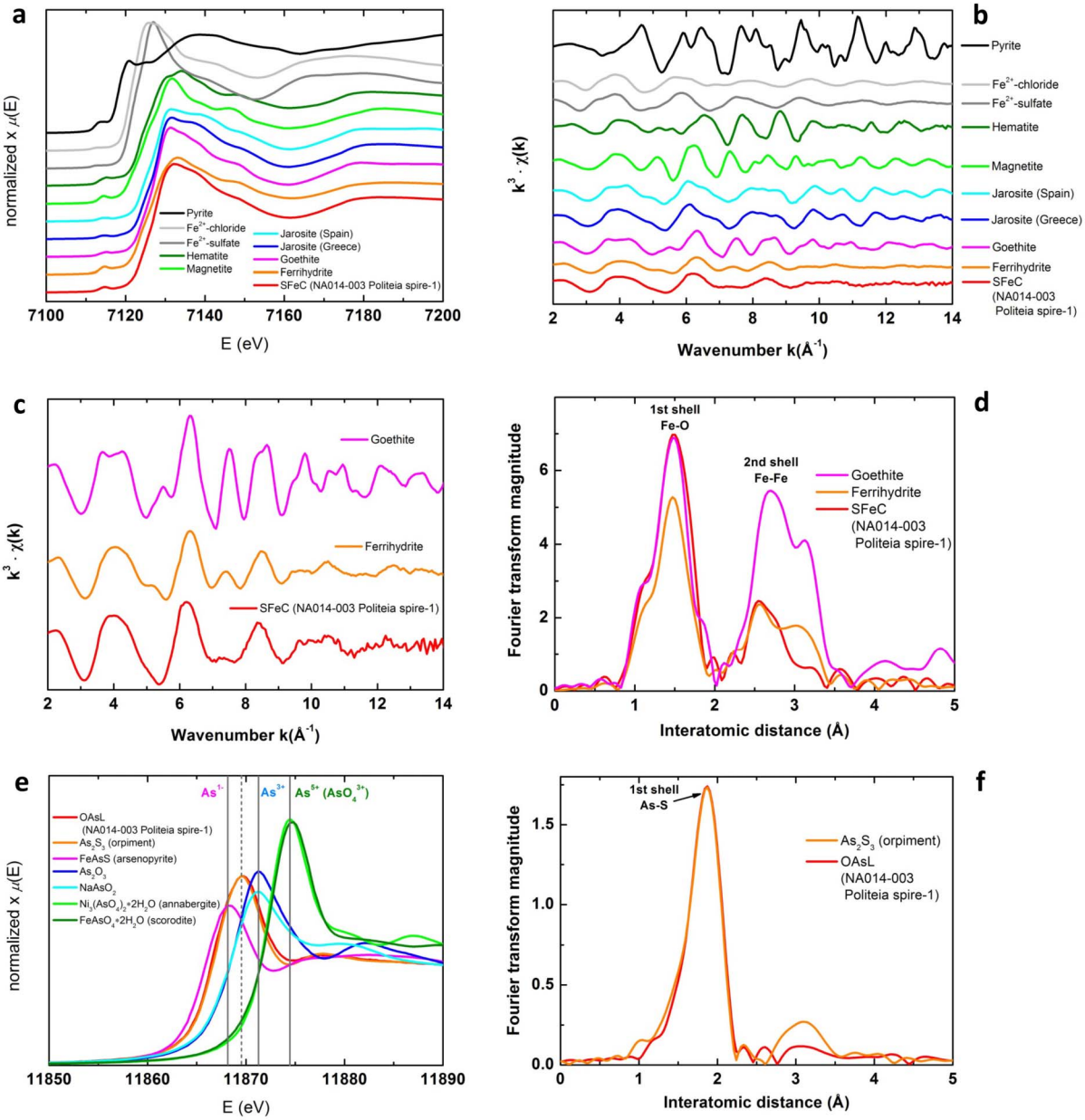

Figure 5 | XAFS spectroscopic data. Normalized (edge jump 1) Fe K-edge XANES spectra of the SFeC material, together with Fe^{+3}-oxide, -ohyxydroxide, - (hydrated)oxyhydroxide, -sulphate (hematite, goethite, ferrihydrite, jarosite) and Fe^{2+} reference materials (pyrite, Fe^{2+}-chloride, Fe^{2+}-sulphate). A natural mixed-valence phase, namely magnetite (Fe_3O_4), is also presented (a). Experimental Fe K-edge EXAFS signal of SFeC material together with the Fe K-edge EXAFS signals of the Fe^{3+} and Fe^{2+} reference materials, as processed using the Athena software (b). The Fourier transform (FT) of the Fe K-edge EXAFS spectrum of the SFeC material together with the FT of Fe-oxyhydroxide (goethite) and Fe-(hydrated) -oxyhydroxide (ferrihydrite) reference materials (c,d). Normalized As K-edge XANES spectra of the OAsL material, in comparison with As_2S_3 (orpiment), FeAsS (arsenopyrite), As_2O_3, $NaAsO_2$, $Ni_3(AsO_4)_2{\cdot}2H_2O$ (annabergite) and $FeAsO_4.2H_2O$ (scorodite) reference materials (e). The Fourier transform (FT) of the As K-edge EXAFS spectrum of the OAsL material together with the FT of the As_2S_3 (orpiment) reference material (f).

= 88.7; see Supplementary Fig. S5) suggests that Hg may be hosted in the observed K-Mg-Al-silicate phases or in other aluminosilicate, or Al-K-Fe-sulphate phases (Supplementary Fig. S3). Thallium concentrations correlate most strongly with As (r = 0.97).

Antimony occurs as Sb-Pb sulphides/sulfosalts and is also associated with pyrite. Gold, Ag, Pb and Sb are characterized by high positive correlation coefficients (similarity level = 79.2) (Supplementary Fig. S5) in the inner sulphide-sulphate core of all samples reflecting the association of these elements with the sulphide phases. The highest concentrations (Au: 32 mg kg^{-1}, Ag: 1,910 mg kg^{-1}, Pb: 6.7 wt%, Sb: 2.2 wt%) occur in samples from "Politeia" (Table 1). The mineralized mound samples, i.e. "Champagne" and "Diffuser II", are distinguished from the Politeia samples by their higher Cu concentrations, 0.15 wt%, and 0.34 wt%, respectively. In contrast, Pb concentrations are highest in the spires and likely indicate differences in fluid temperatures[17]. Moreover, a distinct clustering of samples with respect to these elements is observed between different vent complexes (i.e. "Politeia", "Champagne", Poet's Candle) (Supplementary Fig. S6).

Microbial biodiversity. Studies of microbial diversity on hydrothermal vents have used molecular phylogenetic analyses of small

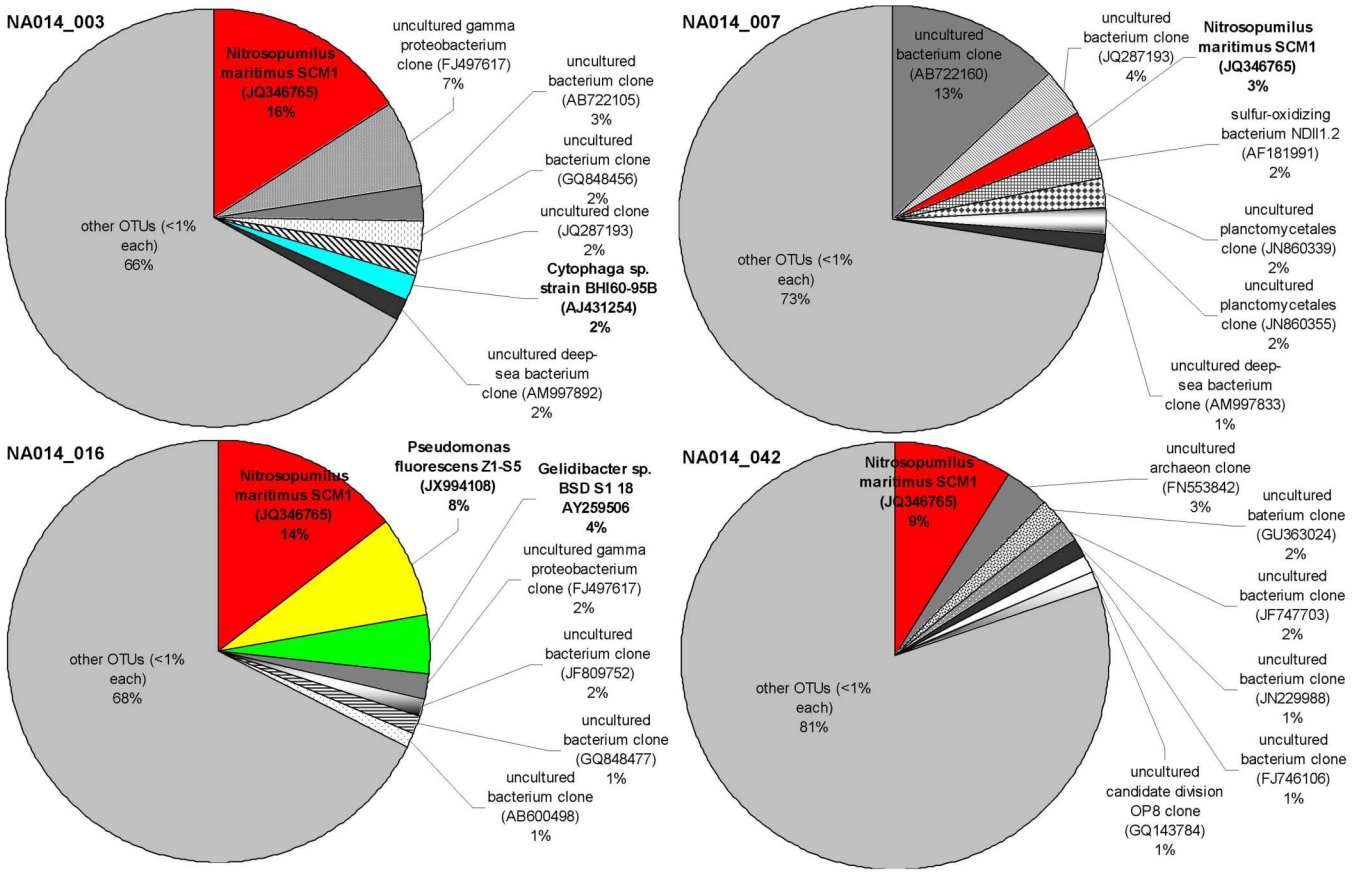

Figure 6 | Microbiological data for Fe microbial mats. Sequence frequency proportion for the most abundant OTUs in the four vent samples (Politeia spire-1: NA014-03, Champagne active mound: NA014-07, Poet's Candle: NA014-16, microbial mat covering the ocean floor: NA014-42). OTUs are represented by their close relatives (>99% sequence similarity; comparison to GenBank entries using BLAST Basic Local Alignment Search Tool, NCBI, Bethesda, MD, USA). Most OTUs were closely related to clones previously retrieved from Fe-rich mats (e.g. clone FJ497617 in NA014-003 and NA014-016), hydrothermal vents (e.g. clones GQ848456 and JQ287193 in NA014-003, AF181991, JN860339 and JN860355 in NA014-007, and FN553842 in NA014-042), massive sulphide deposits (clones AB722105 in NA014-003 and AB722160 in NA014-007) and hydrothermal sulphides (clone JQ28719 in NA014-003).

subunit (SSU) ribosomal RNA (rDNA) gene sequences[29]. Here we used tag pyrosequencing of the V5-V6 hypervariable region of the 16S rRNA gene to assess bacterial and archaeal diversity associated with Fe-rich mat deposits covering Kolumbo's hydrothermal edifices and surrounding seafloor.

A total of 11,566 bacterial and archaeal sequences were obtained, 3,881 from SFeC material covering the "Politeia" (sample NA014-003), 3,070 and 2,394 from similar material covering the "Champagne" (sample NA104-007) and the Poet's Candle (NA014-016), respectively, and 2,221 from a seafloor Fe-mat surrounding "Politeia" (NA014-042) (Fig. 4). In total, 2,757 OTUs (operational taxonomic units) or observed species were found from 22 archaeal and bacterial phyla, 4 candidate divisions and 71 families (Fig. 6 and Supplementary Table S3). The microbial sequences were highly dominated by unidentified members of bacteria and archaea whereas the phylum of *Proteobacteria* was the most dominant bacterial group (Supplementary Table S3). The most abundant OTU (observed species), which was present in all four samples with fractions ranging from 3 up to 16% of the total sequences of the samples (Fig. 6), was closely related (99% sequence similarity) to the mesophilic *Nitrosopumilus maritimus* SCM1, a Thaumarchaeota strain capable of chemoautotrophic growth on ammonia (nitrification) and inorganic carbon (i.e. CO_2) as the sole carbon source[30]. BLAST results revealed that many OTUs were closely related to clones previously retrieved from Fe-rich mats, massive sulphide deposits and hydrothermal sulphides. For example, the most abundant OTU of the "Champagne" (13% of the total sequences of the sample; Fig. 6) was affiliated with an uncultured bacterium clone that was identified in massive sulphide deposits at the Southern Mariana Trough (accession no. AB722160). Microbial assemblages varied significantly among the samples since the similarities occurring at the species level were negligible with a maximum value of 25% recorded between "Politeia" and Poet's candle (Supplementary Table S3).

Discussion

The geodynamic setting of Kolumbo's hydrothermal vent field is atypical of other arc volcanic hydrothermal systems that are commonly associated with arc crust and well-developed back-arc basins (Fig. 1d). Vent samples are uniquely enriched in Sb + Tl + Hg, and they do not conform geochemically to traditional volcanic-associated massive sulphide (VMS) (including Kuroko) deposits. The samples also show epithermal suite geochemical association and enrichment (Au, As, Sb, Hg, Ag, Tl, Ag) (Supplementary Fig. S4). The latter is characteristic of subaerial epithermal and Carlin-type continental deposits[31,32] and has recently been suggested to result from their similar volatile behaviour in subduction systems[33]. Except for the very high contents in Sb and Tl, Kolumbo's style of geochemical enrichment is not unique. Comparable enrichments occur at other seafloor hydrothermal systems, most notably in the Conical Seamount (Lihir island) of the Tabar-Feni arc[34], in the submarine extension of the Taupo Volcanic Zone, (Kermadec arc)[35], at

Palinuro seamount (Tyrrhenian Sea)[36], in the Okinawa trough (JADE field)[37], and the Manus Basin[37]. However, to the best of our knowledge, nowhere else but in Kolumbo such metal enrichment been found in geological forms of hydrothermal spires and mounds[37].

The Kolumbo vent deposits, though seemingly similar to the actively growing Sunrise Kuroko-type deposit, Izu-Bonin arc[38], in terms of pumiceous-hosting and association with submarine-arc front, are different compared to those of Sunrise[39,40]: (i) they occur in different geodynamic environments (see Figs.1c, d); (ii) Sunrise has black smoker chmneys (278°C) with abundant chalcopyrite and amorphous silica; (iii) Sunrise lacks Fe-oxyhydroxide mats; (iv) Kolumbo contains higher concentrations of Sb + Tl(±Hg,Ag), and differs in Au − (Cu + Pb + Zn) − Ag contents (see Supplementary Table S1); (v) Sunrise typifies the association between caldera collapse structures and VMS and (vi) eukaryotic fauna is found at Sunrise, whereas not at Kolumbo.

We suggest that shallow submarine hydrothermal systems, such as those in the Hellenic Volcanic Arc in the Aegean Sea (Aegean arc-type[41]), represent a new hybrid active analogue style of epithermal-VMS mineralization[34,37,41,42] and raise the possibility of similar activity on other submarine volcanoes along the 500 km of the HVA. Moreover, Kolumbo vent field may be characterized by a subseafloor boiling zone, based on: (i) the epithermal-style geochemical enrichment with high and wide ranges in gold-to-base-metal ratios calculated for the different vent complexes (Table 1, and Supplementary Fig. S7); (ii) shallow water (≤600 m) and relatively low temperatures of seafloor venting (≤220°C) near the seawater boiling curve[16] and (iii) the formation of barite-rich spires at the seafloor[17]. Subsea-floor boiling in conjunction with the high volatile content of the Kolumbo rhyolite arc-magma[11], the high gas (CO_2) content of the fluid emissions[10,20], and, the unusually high metal contents (Table 1) may suggest sub-seafloor economic deposition of the epithermal suite of elements including Sb, Tl, Au, Ag, and As[17,37]. The observed metal enrichments also have implications for toxic metal (i.e. Tl, Sb, As, Hg) transport and biogeochemical cycling in seafloor hydrothermal systems, and underscores the importance of submarine volcanic and hydrothermal activity as sources of toxic metals in the oceans.

16S rRNA gene analysis confirmed the presence of highly diverse microbial communities that are spatially associated to the Fe-rich mats dominated by amorphous ferrihydrite-type phases which cover the Politeia spires and the surrounding crater floor. The high variability of microbial community composition reflects the heterogeneity and dynamic nature of these habitats confirming previous investigations[6]. Interestingly, the most dominant observed species (OTU) was not related to Fe-oxidizing bacterial groups that is commonly the case in such low-temperature mats of Fe-oxyhydroxides[14,22,23,25], but instead was closely related to the mesophilic archaeon *Nitrosopumilus maritimus* strain SCM1, capable of chemoautotrophic growth on nitrification, i.e. the ammonium oxidation to nitrite (NO_2^-) and nitrate (NO_3^-), and inorganic carbon as the sole carbon source[43]. This strongly suggests that nitrification is common and the associated microorganisms likely contribute to the carbon and nitrogen cycle in the low-temperature niches of the Kolumbo hydrothermal field[25,43]. This is supported by low pH values (~5) and elevated CO_2 (99 wt%) (ref. 20) in the Kolumbo gas emanations as a source of inorganic carbon, and the correlations between NH_4^+, NO_2^-, NO_3^- and pH in the hydrothermally influenced seawater profile over the active vents of "Champagne" (Fig. 3). Our findings thus extend the marine ecosystems in which nitrifying archaea are important to include acidic hydrothermal vents.

Regardless of a full microbially mediated iron cycle that appears wherever Fe mats flourish[44], microbial growth by iron oxidation and biogenic Fe-(hydrated)-oxyhydroxide formation is difficult to prove in Fe mats, unless microorganisms are "captured in action" of catalyzing Fe oxidation and fixing carbon into cellular biomass and extracellular polymers[45], as it has been uniquely demonstrated by Toner et al.[23]. Consequently, it can only be hypothesized here that, the presence of Fe^{3+}-(hydrated)-oxyhydroxide phases which are morphologically and structurally similar to known biogenic ferrihydrite-type phases, in close association with microbial life within the Fe mats covering the Kolumbo vents, shows microbial intervention in the deposition of Fe^{3+}oxyhydroxide phases[14,22,23,45–48]. Further supporting, yet circumstantial, evidence for the biogenicity of the Fe^{+3} oxyhydroxides comes from positive, and negative, correlations between NH_4^+ and Fe_{FT}, and both NH_4^+ and Fe_{FT} and NO_2^-, respectively, in the hydrothermally influenced seawater profile over the active vents of "Champagne" (Fig. 3). These correlations may suggest a common volcanic/hydrothermal source for reduced species[49] such as NH_4^+ and Fe^{2+}, and a close relationship of Fe with the nitrogen cycle in the vents and ultimately biological nitrification by microbial communities closely related to *Nitrosopumilus maritimus*.

Nitrogen cycling appears to be fertile in biogenic Fe mat communities as demostrated by the omnipresence of microorganisms involved in ammonium (NH_4^+)-nitrite (NO_2^-) nitrate (NO_3^-) redox transformations[44,47]. A biogeochemical relationship between Fe cycling in Fe mats, low-temperature ammonium-oxidizing archaea, and formation of ferrihydrite-type Fe^{3+}-(hydrated)-oxyhydroxides, in acidic hydrothermal vents environment has never been suggested. Ferrihydrite precipitates from the oxidation of Fe^{2+} to Fe^{3+} and rapid hydrolysis of Fe^{3+} (ref. 50). Both abiotic and biological mechanisms may be involved in the oxidation of both soluble and insoluble (solid phase) Fe^{2+} to Fe^{3+} chemical O_2 precipitation under oxic conditions[51], and microbial transformation, respectively[48]. At circumneutral pH in deep sea hydrothermal areas, two major mechanisms are currently implicated in the microbial Fe^{2+} oxidation and formation of ferrihydrite[22,23,45–48]: (i) aerobic Fe^{2+} oxidation by microaerophilic Fe^{2+}-oxidizing bacteria, (ii) anaerobic nitrate-dependent oxidation of Fe^{2+} coupled to nitrate reduction by Fe^{2+}-oxidizing microorganisms. Therefore, linked microbial N- and Fe-cyclings possible in ferruginous fields around hydrothermal vents. However, it has never been demonstrated, neither in the lab nor in the natural environment, how this was possible in an acidified (pH ~ 5) seafloor hydrothermal environment such as Kolumbo[20]. We suggest, that the presence of abundant microbial sequences closely related to nitrifying archaea (i.e. *Nitrisopumilus maritimus*) in the SFeC indicate nitrate production through ammonia biooxidation, in conjunction with virtually absent Fe^{2+}-oxidizing microbes (Fig. 6), and probable anoxic and/or microaerophile conditions, offer a possible alternative and/or parallel mechanism to abiotic/biotic O_2 intervention in the oxidation Fe^{+2} to Fe^{+3} in Fe mats: this is anaerobic nitrate-dependent chemical Fe^{+2} oxidation[47,48] with "biogenic" NO_3^- as an electron acceptor, which would allow for the indirect biogenic precipitation of ferrihydrite-type Fe^{3+}-oxyhydroxide phases at Kolumbo (Fig. 7).

Further clues that microbial biogeochemical processes extend towards the interior of the Kolumbo vents are provided by: (i) the existence of sharp microscale redox gradients, and sharp mineralogical boundaries in the Kolumbo spires, suggesting microbially-induced chemical disequilibria for metabolic energy gain[48]; this is evidenced by the occurrence of reduced forms of As in the form of orpiment (As_2S_3)-type" phases (Fig. 5e,f) in the OAsL material underlying the SFeC (Fig. 4a); and, (ii) The structural and morphological similarity of Kolumbo's amorphous orpiment (As_2S_3)-type phases (Fig. 4c, 5e,f) with biologically produced polycrystalline As^{+3}-S from initially amorphous biogenic $As^{+5}{}_2S_3$ (ref. 28), that may suggest biologically controlled redox cycling of As in the OAsL material[28,52].

We conclude that Kolumbo's unique geodynamic setting is balanced by polymetallic hydrothermal vent mineralization uniquely enriched in Tl and Sb, a vent ecosystem dominated by archaeal sequences closely related to *Nitrosopumilus maritimus* strongly

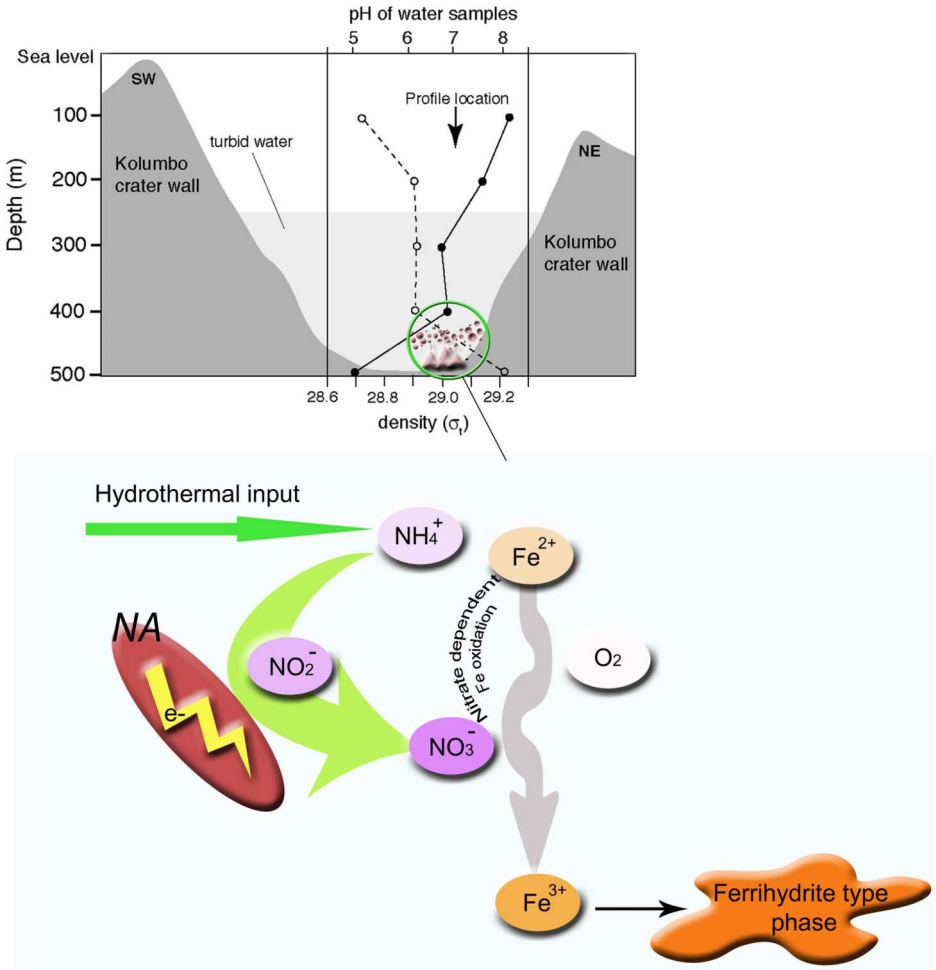

Figure 7 | A simplified model for biogenic formation of ferrihydrite-type Fe^{3+}- (hydrated) oxyhydroxides at acidic shallow-submarine hydrothermal vents. Nitrate (NO_3^-) is biologically produced through hydrothermal ammonium (NH_4^+) biooxidation by abundant nitrifying archaea (*NA*). Large-scale anaerobic nitrate-dependent chemical oxidation of hydrothermal Fe^{2+} with microbially produced NO_3^- as an electron acceptor allows for the indirect biogenic precipitation of ferrihydrite$^+$type phases at Kolumbo's low$^+$temperature hydrothermal vent niches. A parallel small$^+$scale mechanism of abiotic molecular O_2 intervention in the oxidation Fe^{2+} to Fe^{3+} cannot be excluded. Schematic cross section of Kolumbo's crater with pH (solid circles) and density (open circles) profiles is modified after Carey et al.[20]. Hydrothermal spires not to scale.

suggesting that nitrification is common in this environment, and a biogeochemical interplay between Fe and N (Fig. 7) in low-temperature Fe microbial mats, distinct among seafloor hydrothermal systems known anywhere in the world.

Methods

Submarine Reconnaissance. The Exploration Vessel (E/V) *Nautilus* is a 64-meter research vessel, owned and operated by the Ocean Exploration Trust (O.E.T.). *Nautilus* is equipped with the remotely operated vehicles (ROVs) *Hercules*, *Argus*, operated by the Institute for Exploration. The Hercules and Argus system is a state-of-the-art deep sea robotic laboratory capable of exploring depths up to 4,000 meters. Each remotely operated vehicle (ROV) is equipped with a dedicated suite of cameras and sensors that receive electrical power from the surface through a fiber-optic cable, which also transmits data and video. A 20-hp electric/hydraulic pump powers the mechanical functions on *Hercules*. Two manipulator arms, one dexterous and the other strong, work together to sample and move equipment around on the seafloor. It is also equipped with a number of tools, including a suction sampler, sampling boxes with actuating trays, and sediment coring equipment, as well as several other purpose-built tools for different scientific objectives. The ROV *Hercules* is equipped with a suite of mapping instruments that enable detailed visual and acoustic seafloor surveys. The mapping sensors include a 1,375 kHz BlueView Technologies multibeam, verged color and black and white 12-bit 1360 × 1024 Prosilica stereo cameras, and a 100 mW 532 nm green laser sheet. The sensors are mounted near the rear of vehicle and arranged to image a common area. The vehicle navigation data comes from an RDI Doppler velocity log (DVL), IXSEA OCTANS fiber-optic gyroscope, and a Paroscientific depth sensor. The multibeam bathymetric surveys were carried out by the R/V Aegaeo of the Hellenic Centre for Marine Research, using a SEABEAM 2120 swath system. The SEABEAM 2120 is a hull-mounted swath system operating at 20 kHz in water depths not exceeding 6,000 m.

Sample collection. Two massive sulphide-rich spires, Politeia spire-1 and Politeia spire-2 (sample NA014-003 and NA014-039)), were recovered from the Politeia Vent Complex at ~500 m depth by ROV Hercules. Four hydrothermal mound samples were collected from active vents: three from the Champagne Vent Complex (samples NA014-007, NA014-027 and NA014-028), and one from the Diffuser II Vent Complex (sample NA014-005) accomplished with the Hercules ROV using grab. .Water samples were collected during cruise NA-014 using Niskin bottles on the ROV Hercules and in specially designed pressure-tight containers that allowed for gas retention during ascent to the surface. Vertical profiling was conducted over Champagne vent (samples NA014023, NA014010, NA014009, NA014046, NA014008). Two additional samples (NA01432 and NA01433) were collected from the south side of the crater, an area without obvious hydrothermal activity, for comparison.

Powder X-ray diffraction. The solid materials collected by the ROV *Hercules* were initially sub-sampled on-board for mineralogical, chemical and microbiological characterization. Powder X-ray diffraction patterns (PXRD) were obtained using a Siemens D5005 (currently Bruker AXS) diffractometer with CuKα radiation (λ = 1.54 Å) at an accelerating voltage of 40 kV. The identification of crystalline phases was obtained with data from ICDD and the evaluation was performed with EVA software from Siemens (currently Bruker AXS) for semi-quantitative analysis.

Scanning electron microscopy. Scanning Electron Microscopy – Energy Dispersive Spectrometry (SEM-EDS) investigation of carbon-coated free surfaces and polished (in epoxy resin) solid samples was performed using a Jeol JSM-5600 SEM equipped with an Oxford EDS.

X-ray absorption fine structure (XAFS) spectroscopy. The Fe-(hydrated)-oxyhydroxide and As-sulphide PXRD-amorphous phases, namely SFeC and OAsL (Fig. 4) covering the surface of Politeia spire-1/NA014-003, were characterized by X-ray absorption fine structure (XAFS) spectroscopy at the SUL-X beamline of ANKA Synchrotron facility (KIT, Germany). XAFS spectra of sample OAsL were obtained from fine-grained material pressed with cellulose to pellets. Spectra were measured at the As K-edge (11867 eV). Arsenopyrite (FeAsS), natural orpiment (As_2O_3), natural arsenates (scorodite: $FeAsO_4.2H_2O$ and annabergite: $Ni_3(AsO_4)_2.8H2O$) as well as synthetic As_2O_3 and $NaAsO_2$, were used as reference materials of various As species. The spectra were processed using the Athena software[53]. Spectra of sample SFeC, were measured at the Fe K-edge (7112 eV) using natural pyrite (FeS_2), natural Fe oxides (magnetite: Fe_3O_4 and hematite: Fe_2O_3), synthetic Fe oxyhydroxides and (hydrated)-oxyhydroxides (goethite: FeOOH and ferrihydrite: $Fe_{10}O_{14}(OH)_2.\chi H_2O$), natural jarosite ($KFe_3(OH)_6(SO4)_2$) and synthetic Fe^{2+}-chloride and -sulphate as reference materials. Energy was calibrated for the As K-edge XAFS measurements to 11.919 eV (1st derivative of the Au L3 edge, Au metal foil), and for Fe K-edge XAFS measurements to 7.112 eV (1st derivative of the Fe K edge, Fe metal foil).

Whole rock elemental analysis of vent samples. Seven samples (NA014-003ISSC, NA014-003OAsL, NA014-003SFeC, NA014-027, NA014-028, NA014-039ISSC, NA014-039SFeC) were air-dried and pulverized using an agate mortar. Bulk analyses for major and trace elements were performed using a Perkin Elmer ICP-OES and a Perkin Elmer Sciex Elan 9000 ICP-MS following a $LiBO_2/LiB_4O_7$ fusion and HNO_3 digestion of a 0.2 g sample. In addition, a separate 0.5 g split was digested in a HNO_3:HCl mixture (1 : 3) –aqua regia- and analysed by ICP-MS for precious and base metals. The bulk (total) sulfur content was determined using a Leco elemental analyzer. Analytical quality control procedures included analysis of 1 duplicate (NA014-028), 2 blank solutions as well as analysis of a series of appropriate reference materials (OREAS45CA, DS8, DOLOMITE-2, SO-18, GS311-1, GS910-4). Seven additional 5 g splits of samples (NA014-003 composite, NA014-005, NA014-007, NA014-016, NA014-027, NA014-028, NA014-039composite) were digested in aqua regia and analyzed by flame atomic absorption spectroscopy (AAS) to determine high concentrations of metals which exceeded the upper limits of ICP-OES/MS. Gold concentrations were measured by graphite-furnace AAS (GF-AAS) after leaching the digested samples with methyl isobutyl ketone (MIBK). One sample (NA014-003) was analyzed in duplicate. A blank sample and the certified material SP49 were analyzed in the same batch with the samples for analytical quality control. Total organic carbon was determined by the Walkey Black method.

pH. The pH was measured in situ with a YSI 63 salinometer/pH meter and all samples were filtered through 0.45 μm millipore membrane filters using peristaltic pumps.

Nitrogen species and iron. The concentration of nitrogen species NH_4^+, NO_2^-, NO_3^- were determined with standard spectrophotometric methods[54] employing a Varian Carry 1E spectrophotometer while concentrations of 0.45 μm filterable Fe_{FT} were determined by Flame Atomic Absorption Spectrometry (VARIAN Model SpectrAA-200) after preconcentration of the sample by the use of a Chelex-100 resin column, according to a slight modification of the Riley and Taylor method[55].

16S rRNA gene sequence analysis. Upon return to the surface, solid materials and push corer collected by the ROV *Hercules* were carefully sub-sampled for microbial community analysis. Samples were carefully collected by scraping the surface of the spires with a sterile scalpel and were placed in sterile Petri dishes. For the push-corer sample, the surface orange to brown coloured mat (0–2 cm) was carefully removed with a sterile syringe and was placed in a 50 ml-falcon tube. All microbiological samples were kept frozen at −20°C until further processing in the laboratory. Total microbial community DNA was extracted from approximately 1 g of material of microbial mat by employing the MoBio UltraClean Soil DNA isolation kit (MoBio Laboratories, Carlsbad, CA, USA) as recommended by the manufacturer. DNA concentrations were quantified by using the NanoDrop ND-1000 UV-Vis Spectrophotometer (NanoDrop Technologies, USA). The V5-V6 region of the 16S rRNA gene was amplified by PCR. The PCR reaction mixture (final volume of 15 μl) contained 5 μl of 5× KAPA HiFi Fidelity buffer (contains 2.0 mM Mg^{2+} at 1×), 0.75 μl of KAPA dNTP Mix (10 mM each dNTP), ~10 g of template DNA and 0.50 μl of KAPA HiFi HotStart DNA Polymerase (1 U/μl) (KAPA Biosystems). The V5-V6 region was amplified with the following set of primers: 802f (5′-GATTAGATACCCBNGTA-3′) and 1027r (5′-CGACRRCCATGCANCACCT-3′). The following thermal cycling program was applied: initial denaturation at 95°C for 5 min, 30 cycles of denaturation at 98°C for 20 sec, primer annealing at 55°C for 15 sec, and extension at 72°C for 30 sec followed by a final extension at 72°C for 5 min. Quantification of the PCR products was performed using the SYBR Green stain and a QuantiFluor spectrophotometer (Promega). The sequences of the partial 16S rRNA genes were produced in the labs of the Institute of Marine Biology, Biotechnology and Aquaculture of the Hellenic Centre for Marine Research (Crete, Greece) by using a Roche GS-FLX 454 pyrosequencer (Roche, Mannheim, Germany) following the instructions of the manufacturer for amplicon sequencing. Sequences that were shorter than 200 bp in lengths were removed. Taxonomy was assigned using the RDP classifier of the Ribsomal Database Project. Pyrosequencing noise was removed by using the denoiser program. Sequences were assigned to observed species also known as operational taxonomic units (OTUs) using the QIIME software at 3% sequence divergence (species level). Similarity analysis among the samples was carried out using PRIMER 6.1.5 software. Pyrosequencing data were submitted to NCBI Sequence Read Archive with the study accession number SRA054862.

1. Papanikolaou, D. Geotectonic evolution of the Aegean. *Bull. Geol. Soc. Greece* **27**, 33–48 (1993).
2. Royden, L. H. & Papanikolaou, D. J. Slab segmentation and late Cenozoic disruption of the Hellenic arc. *Geochem. Geophys. Geosyst.* **12** (2011).
3. Le Pichon, X. & Angelier, J. The Hellenic Arc and Trench system: A key to the neotectonic evolution of the Eastern Mediterranean area. *Tectonophysics* **60**, 1–42 (1979).
4. Kearey, P., Klepeis, K. A. & Vine, F. Global Tectonics (3rd ed), 482 pp. (Wiley-Blackwell, John Wiley & Sons, West Sussex UK, 2009).
5. Nomikou, P. *et al.* Submarine volcanoes of the Kolumbo volcanic zone NE of Santorini Caldera, Greece. *Global Planet. Change* **90–91**, 135–151 (2012).
6. Holden, J. F., Breier, J. A., Rogers, K. L., Schulte, M. D. & Toner, B. M. Biogeochemical processes at hydrothermal vents: Microbes and minerals, bioenergetics, and carbon fluxes. *Oceanography* **25**(1), 196–208 (2012).
7. Southam, G. & Saunders, J. A. The geomicrobiology of ore deposits. *Econ. Geol.* **100**, 1067–1084 (2005).
8. Forster, M. A. & Lister, G. S. Detachment faults in the Aegean core complex of Ios, Cyclades, Greece. In: Exhumation Processes: Normal Faulting, Ductile Flow and Erosion. (eds, Ring, U., Brandon, M. T., Lister, G. S. & Willett, S. D.). *Spec. Publ. Geol. Soc. London* **154**, 305–324 (1999).
9. Nomikou, P. *et al.* Submarine volcanoes along the Aegean volcanic arc. *Tectonophysics* **597**, 123–146 (2012).
10. Carey, S. *et al.* Exploration of the Kolumbo Volcanic Rift Zone. In Bell, K. L. C. & Fuller, S. A. eds. New Frontiers in Ocean Exploration: The E/V Nautilus 2010 Field Season. *Oceanography* **24**(1), supplement (2011).
11. Cantner, K. A. Volcanologic and petrologic analysis of the 1650 AD submarine eruption of Kolumbo Volcano, Greece. MS Thesis. *University of Rhode Island* (2010).
12. Sigurdsson, H. *et al.* Marine Investigations of Greece's Santorini Volcanic Field. *EOS Trans. AGU* **87**, 337–339 (2006).
13. Roman, C. *et al.* The development of high-resolution seafloor mapping techniques: In Bell, K. L. C., Elliott, K., Martinez, C. & Fuller, S. A. eds 2012. New Frontiers in Ocean Exploration: The E/V Nautilus and NOAA Ship Okeanos Explorer 2011 Field Season. *Oceanography* **25**(1), 42–45 (2012).
14. Edwards, K. J. *et al.* Ultra-diffuse hydrothermal venting supports Fe-oxidizing bacteria and massive umber deposition at 5000 m off Hawaii. *ISME J.* **5**, 1748–1758 (2011).
15. Fouquet, Y. *et al.* Metallogenesis in back-arc environments: the Lau Basin example. *Econ. Geol.* **88**, 2154–2181 (1993).
16. Tivey, M. Generation of seafloor hydrothermal vent fluids and associated mineral deposits. *Oceanography* **20**, 50–65 (2007).
17. Hannington, M. D., De Ronde, C. E. J. & Petersen, S. Sea-floor Tectonics and Submarine Hydrothermal Systems (eds Hedenquist, J. W., Thompson, J. F. H., Goldfarb, R. J. & Richards, J. D.) *Econ. Geol. 100th Anniv. Vol.*, 111–141 (2005).
18. Stoffers, P. *et al.* Submarine volcanoes and high-temperature hydrothermal venting on the Tonga arc, southwest Pacific. *Geology* **34**, 453–456 (2006).
19. Hannington, M. *et al.* First observations of high-temperature submarine hydrothermal vents and massive anhydrite deposits off the north coast of Iceland. *Mar. Geol.* **177**, 199–220 (2001).
20. Carey, S. *et al.* CO_2 degassing from hydrothermal vents at Kolumbo submarine volcano, Greece and the accumulation of acidic crater water. *Geology* doi:10.1130/G34286.1 (2013).
21. Westall, F. *et al.* The 3.466 Ga Kitty's Gap chert, an Early Archaean microbial ecosystem. In Reimold, W. U. & Gibson, R. (eds). *GSA Special Paper* **405**, 105–131 (2006a).
22. Edwards, K. J., McCollom, T. M., Konishi, H. & Buseck, P. R. Seafloor bioalteration of sulfide minerals: Results from in situ incubation studies. *Geochim. Cosmochim. Acta* **67**, 2843–2856 (2003).
23. Toner, B. M. *et al.* Biogenic iron oxyhydroxide formation at mid-ocean ridge hydrothermal vents: Juan de Fuca Ridge. *Geochim. Cosmochim. Acta* **73**, 388–403 (2009).
24. Peng, X. *et al.* Intracellular and extracellular mineralization of a microbial community in the Edmond deep-sea vent field environment. *Sediment. Geol.* **229**, 193–206 (2010).
25. Li, J. *et al.* Microbial diversity and biomineralization in low-temperature hydrothermal iron–silica-rich precipitates of the Lau Basin hydrothermal field. *FEMS Microbiol. Ecol.* **81**, 205–216 (2012).
26. Jones, B., de Ronde, C. E. J. & Renaut, R. W. Mineralized microbes from Giggenbach submarine volcano. *J. Geophys. Res.* **113**, 13 (2008).
27. Oakes, M. *et al.* Characterization of iron speciation in single particles using XANES spectroscopy and micro X-ray fluorescence measurements: insight into factors controlling iron solubility. *Atmos. Chem. Phys.* **12**, 745–756 (2012).
28. Lee, J. H. *et al.* Biogenic formation of photoactive arsenic-sulfide nanotubes by Shewanella sp. strain HN-41. *P. Natl. Acad. Sci. USA* **104**, 20410–20415 (2007).
29. Zinger, L. *et al.* Global patterns of bacterial beta-diversity in seafloor and seawater ecosystems. *PLOS ONE* **6**, (2011).

30. Labrenz, M. *et al*. Relevance of a crenarchaeotal subcluster related to Candidatus Nitrosopumilus maritimus to ammonia oxidation in the suboxic zone of the central Baltic Sea. *ISME J.* **4**, 1496–1508 (2010).
31. Cooke, D. R. & Simmons, S. F. Characteristics and genesis of epithermal gold deposits. *Econ. Geol. Rev.* **13**, 221–244 (2000).
32. Muntean, J. L., Cline, J. S., Simon, A. C. & Longo, A. A. Magmatic-hydrothermal origin of Nevada's Carlin-type gold deposits. *Nat. Geosci.* **4**, 122–127 (2011).
33. Saunders, J. A. & Brueseke, M. E. Volatility of Se and Te during subduction-related distillation and the geochemistry of epithermal ores of the western United States. *Econ. Geol.* **107**, 165–172 (2012).
34. Petersen, S., Herzig, P. M., Hannington, M. D., Jonasson, I. R. & Arribas, A. Jr. Submarine Gold Mineralization Near Lihir Island, New Ireland Fore-Arc, Papua New Guinea. *Econ. Geol.* **97**, 1795–1813 (2002).
35. Stoffers, P. *et al*. Elemental mercury at submarine hydrothermal vents in the Bay of Plenty, Taupo volcanic zone, New Zealand. *Geology* **27**, 931–934 (1999).
36. Monecke. *et al*. Shallow submarine hydrothermal systems in the Aeolian volcanic arc. *Italy EOS Trans. AGU* **90**, 110–111 (2009).
37. Hannington, M. D., Poulsen, K. H., Thompson, J. F. H. & Sillitoe, R. H. Volcanogenic gold in the massive sulfide environment. In Barrie, C. T. & Hannington, M. D. (eds) Volcanic-associated massive sulfide deposits: processes and examples in modern and ancient settings. *Econ. Geol. Rev.* **8**, 325–356 (1999).
38. Iizasa, K. *et al*. A Kuroko-Type polymetallic sulfide deposit in a submarine silicic caldera. *Science* **283**, 975–977 (1999).
39. Watanabe, K. & Kajimura, T. The hydrothermal mineralization at Suiyo seamount, Izu-Ogasawara arc. *Resour. Geol.* **44**, 133–140 (1994).
40. Stix, J. *et al*. Caldera-forming processes and the origin of submarine volcanogenic massive sulfide deposits. *Geology* **31**, 375–378 (2003).
41. Naden, J., Kilias, S. P. & Darbyshire, D. P. F. Active geothermal systems with entrained seawater as modern analogs for transitional volcanic-hosted massive sulfide and continental magmato-hydrothermal mineralization: The example of Milos Island, Greece. *Geology* **33**, 541–544 (2005).
42. Sillitoe, R. H. & Hedenquist, J. W. Linkages between volcanotectonic settings, or fluid compositions, and epithermal precious metal deposits. *Econ. Geol. Soc. Spec. Publ.* **10**, 315–343 (2003).
43. Walker, C. B. *et al*. Nitrosopumilus maritimus genome reveals unique mechanisms for nitrification and autotrophy in globally distributed marine crenarchaea. *P. Natl. Acad. Sci. USA* **107**, 8818–8823 (2010).
44. Chi Fru, E., Piccinelli, P. & Fortin, D. Insights into the Global Microbial Community Structure Associated with Iron Oxyhydroxide Minerals Deposited in the Aerobic Biogeosphere. *Geomicrobiology* **29**, 587–610 (2012).
45. Templeton, A. S. Iron in Earth Surface Systems: Geomicrobiology of Iron in Extreme Environments. *Elements* **7**, 95–100 (2011).
46. Toner, B. M. *et al*. Mineralogy of iron microbial mats from Loihi Seamount. *Front. Microbiol.* **3**, 1–18 (2012).
47. Weber, K. A., Achenbach, L. A. & Coates, J. D. Microorganisms pumping iron: Anaerobic microbial iron oxidation and reduction. *Nat. Rev. Microbiol.* **4**(10), 752–764 (2006).
48. Konhauser, K. O., Kappler, A. & Roden, E. Iron in microbial metabolism. *Elements* **7**(2), 89–93 (2011).
49. Santana-Casiano, J. M. *et al*. The natural ocean acidification and fertilization event caused by the submarine eruption of El Hierro. *Sci. Rep.* **3**, 1140; DOI:10.1038/srep01140 (2013).
50. Jambor, J. L. & Dutrizac, J. E. Occurrence and constitution of natural and synthetic ferrihydrite, a widespread iron oxyhydroxide. *Chem. Rev.* **98**, 2549–2585 (1998).
51. Posth, N. R., Konhauser, K. O. & Kappler, A. Banded Iron Formations. In Reitner J. & Thiel V. (Eds) Encyclopedia of Geobiology. *Springer*, 92–103.
52. Oremland, R. S. & Stolz, J. F. The ecology of arsenic. *Science* **300**, 939–944 (2003).
53. Ravel, B. & Newville, M. ATHENA, ARTEMIS, H*EPHAESTUS: data analysis for X-ray absorpt*ion spectroscopy using IFEFFIT. *J. Synchrotron Radiat.* **12**, 537–541 (2005).
54. Stricland, J. D. H. & Parsons, T. R. Fisheries Research Board of Canada. A Practical Handbook of Seawater Analysis. 49–52, 65–70, 71–76, 77–80 (1968).
55. Scoullos, M. & Dassenakis, M. Determination of dissolved metals in seawater, using the resin Chelex-100. Proceedings of the 1st Greek Symposium on Oceanography and Fisheries. 302–309 (1984).

Acknowledgments

Support for the operation of the E/V *Nautilus* was provided by the U.S. National Oceanic and Atmospheric Administration (NA06OAR4600140, NA10OAR4600127), Office of Ocean Exploration (OCE-0452478), and the Ocean Exploration Trust. The officers and the crew of the E/V *Nautilus* are gratefully acknowledged for their important and effective contribution to the field work and sampling. We acknowledge funding from the Special Account for Research Grants, National and Kapodistrian University of Athens (70/4/11078, 70/3/11401) and the Karlsruhe Institute of Technology-ANKA Synchrotron Radiation Facility (ENV-199). Bell K.L.C., Chief Scientist of Nautilus Programme and Vice Precident of O.E.T. (Ocean Exploration Trust) is greatly acknowledged for operational support and her participation in data collection. Microbiological analysis was supported by the Hellenic Centre for Marine Research -Crete Department, Greece.

Author contributions

S.P.K., P.N., S.C., D.P., A.G. and M.S. designed and organized research; K.C.B. and P.N. were the Co-Chief Scientists on board NA014; A.G., P.N.P., E.S., K.B. and I.L. participated to the NA014 Expedition (Hellenic Arc) of E/V Nautilus and contributed to sampling and on-board measurements; D.P. performed the geodynamic profile of the studied area; P.N. and I.L. the bathymetric maps of Kolumbo volcano and vent field; A.G., P.G. and S.P.K. managed the basic (PXRD, SEM-EDS) mineralogical characterization of the solid samples; A.G., T.J.M., P.G., J.G. and R.S. undertook the Synchrotron-based characterization of the PXRD-amorphous As- and Fe-phases, while P.G. carried out the XAFS data evaluation; A.A., S.P.K., A.G., M.S., E.S. and P.G. managed the major and trace-element geochemical characterization of the solid samples. E.S. performed the chemical analyses of the seawater samples on board and on the laboratory and M.S. contributed to the interpretation and writing of the chemical results. P.N.P. and C.C. performed the microbiological characterization of the solid samples; S.P.K., P.N., D.P., A.A., A.G. and P.P. wrote the paper; all authors contributed to interpretation of the results and editing of the manuscript.

Additional information

Supplementary information accompanies this paper at http://www.nature.com/scientificreports

Competing financial interests: The authors declare no competing financial interests.

How to cite this article: Kilias, S.P. *et al*. New insights into hydrothermal vent processes in the unique shallow-submarine arc-volcano, Kolumbo (Santorini), Greece. *Sci. Rep.* **3**, 2421; DOI:10.1038/srep02421 (2013).

Title: New insights into hydrothermal vent processes in the unique shallow-submarine arc-volcano, Kolumbo (Santorini), Greece

Authors: Stephanos P. Kilias[1], Paraskevi Nomikou[1], Dimitrios Papanikolaou[1], Paraskevi N. Polymenakou[2], Athanasios Godelitsas[1], Ariadne Argyraki[1], Steven Carey[3], Platon Gamaletsos[1,6], Theo J. Mertzimekis[4], Eleni Stathopoulou[5], Joerg Goettlicher[6], Ralph Steininger[6], Konstantina Betzelou[1], Isidoros Livanos[1], Christos Christakis[1,2], Katherine Croff Bell [3], Michael Scoullos[5]

Affiliations:

[1]National and Kapodistrian University of Athens, Faculty of Geology and Geoenvironment, Panepistimiopoli Zografou, 15784 Athens, Greece.

[2]Hellenic Centre for Marine Research, Institute of Marine Biology, Biotechnology and Aquaculture, Gournes Pediados, P.O.Box 2214, Gr 71003, Heraklion Crete, Greece.

[3]Graduate School of Oceanography, University of Rhode Island, Narragansett,USA.

[4]National and Kapodistrian University of Athens, Faculty of Physics, Panepistimiopoli Zografou, 15784 Athens, Greece.

[5]National and Kapodistrian University of Athens, Faculty of Chemistry, Panepistimiopoli Zografou, 15784 Athens, Greece.

[6] Karlsruhe Institute of Technology, ANKA Synchrotron Radiation Facility, Hermann-von-Helmholtz-Platz 1, 76344 Eggenstein-Leopoldshafen, Germany

***Correspondence:** Correspondence and requests for materials should be addressed to S.P.K.. (email: kilias@geol.uoa.gr).

This supplement contains:

1. **Supplementary Figures (7)**
2. **Supplementary Tables (4)**
3. **Supplementary References**

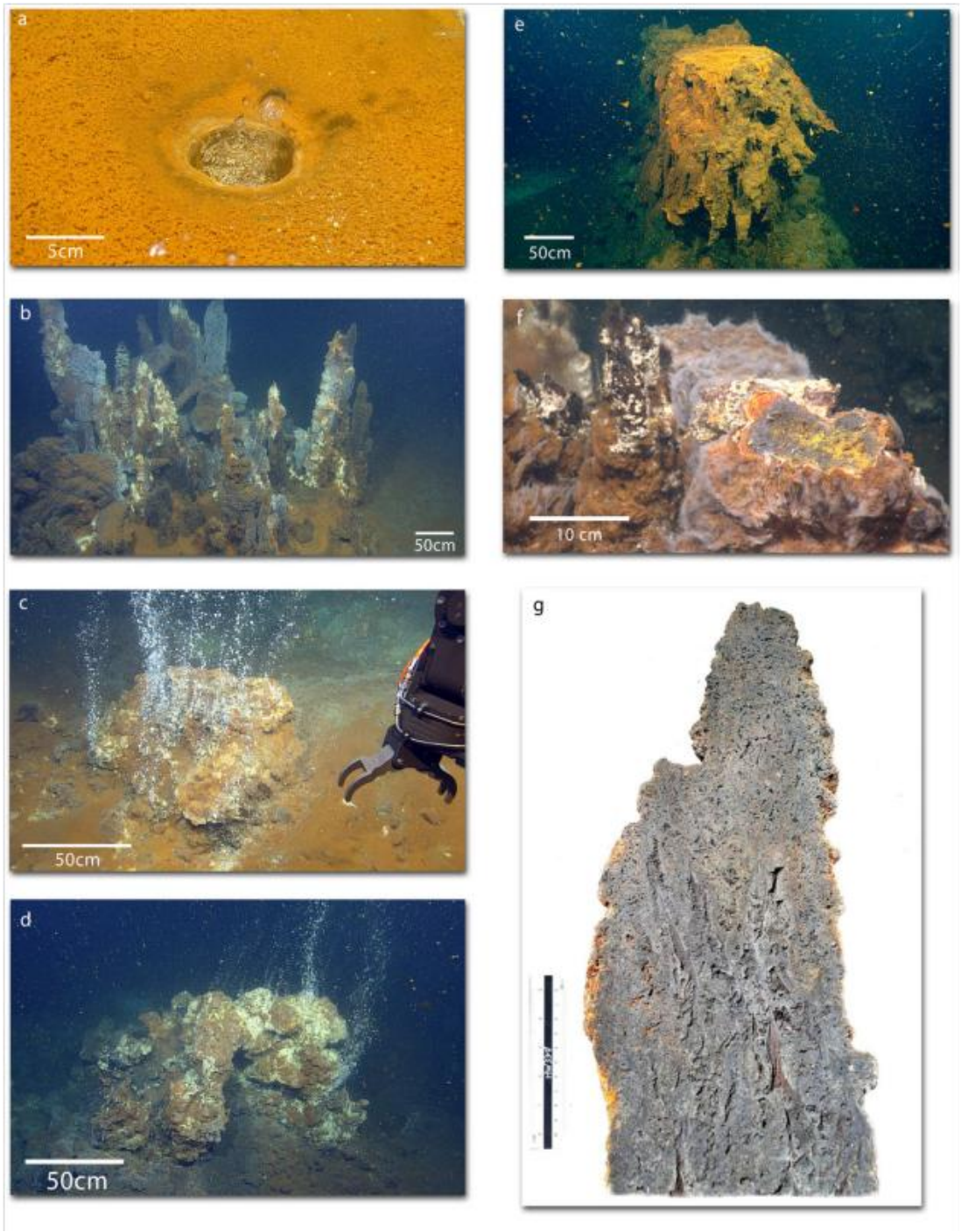

Supplementary Figure 1| Bottom photographs from ROV Hercules submersible and single intact recovered chimney (Submarine photographs taken by co-Chief Scientists Steven Carey, Katherine Croff Bell, Paraskevi Nomikou onboard E/V Nautilus during oceanographic cruises NA007-NA014). **a,** Small pockmark–like crater discharging low-temperature (70°C) fluids. **b**, Politeia Vent Complex("Politeia"): Field of multiple inactive and active sulphide/sulphate , spires

up to 2 m high on top of a hydrothermal mound with spire fragments draped by Fe-bearing bacterial mats.Clear fluids vent from active spires (not visible). **c**, The base of the knocked over vent spire sample NA014-003, revealing textural zones (see Figure 5a). The exterior of the spire is covered by grayish active suspended filamentous microbial biofilms (streamers). Note the "flame-like" jets of hydrothermal steam on far back spire (left corner). **d**, Champagne Vent Complex("Champagne"): Active high-temperature (220°C) vent discharging both gases (>99 % CO_2) and fluids. **e**, Diffuser II Vent Complex("Diffuser II": Vent with bacterial covering and gas bubbling. **f**, Poet's Candle: The largest observed (height ~ 4 m) inactive vent with bacterial covering. **g**, Section of the NA014-003 single intact spire. Bar is 10 cm long.

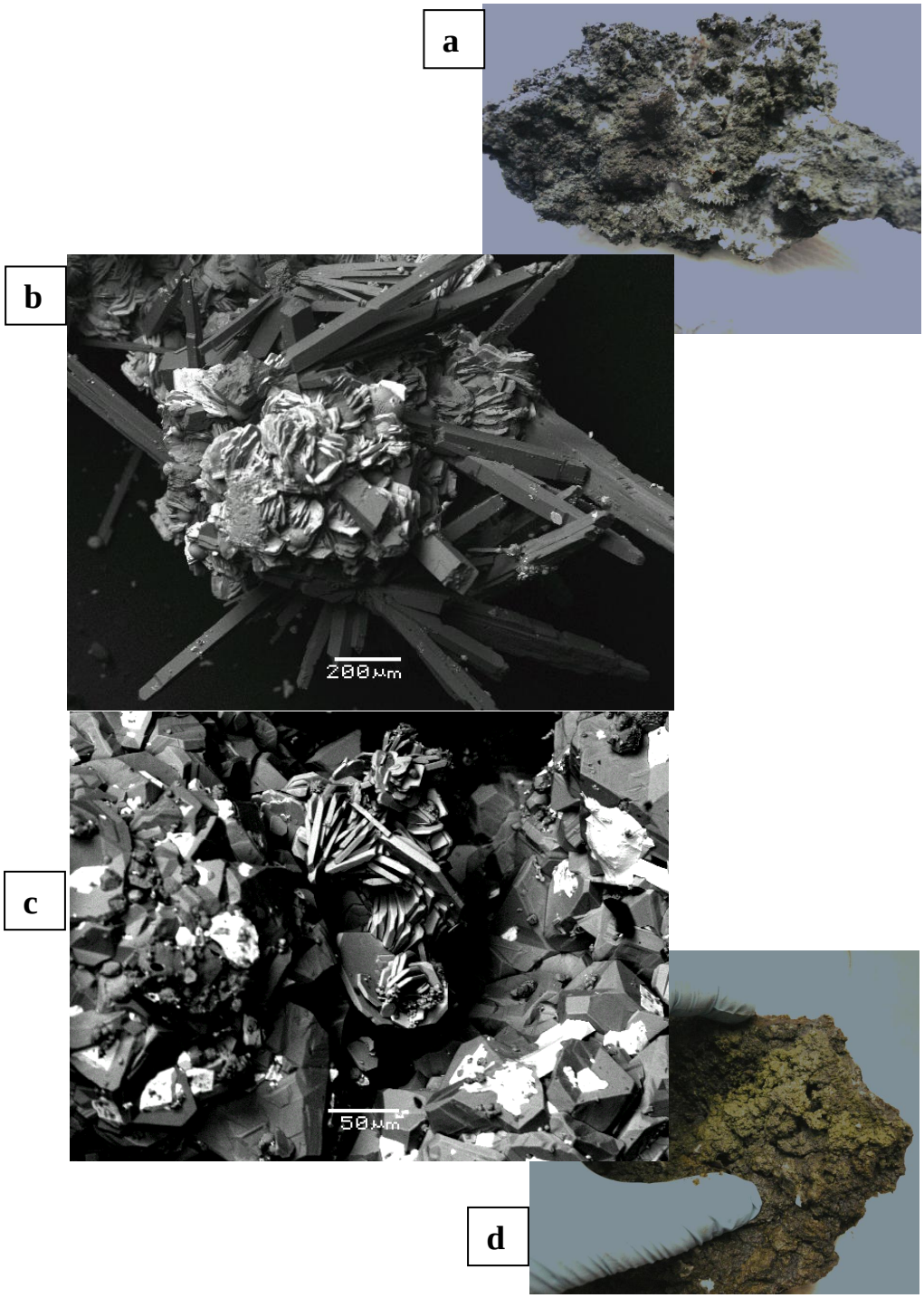

Supplementary Figure 2/ Macroscopic and SEM images of sulfide-sulfate minerals from Champagne . a, hand specimen with gypsum acicular crystals grown onto sulphide-sulphate matrix, **b,** SEMimage of external surface of the sample showing botryoidal aggregates of pyrite and/or marcasite, associated with euhedral crystals of gypsum and barite, **c,** local aggregates of twinned chalcopyrite crystals with barite aggregates and galena precipitates, **d**, mount piece with brassy chalcopyrite

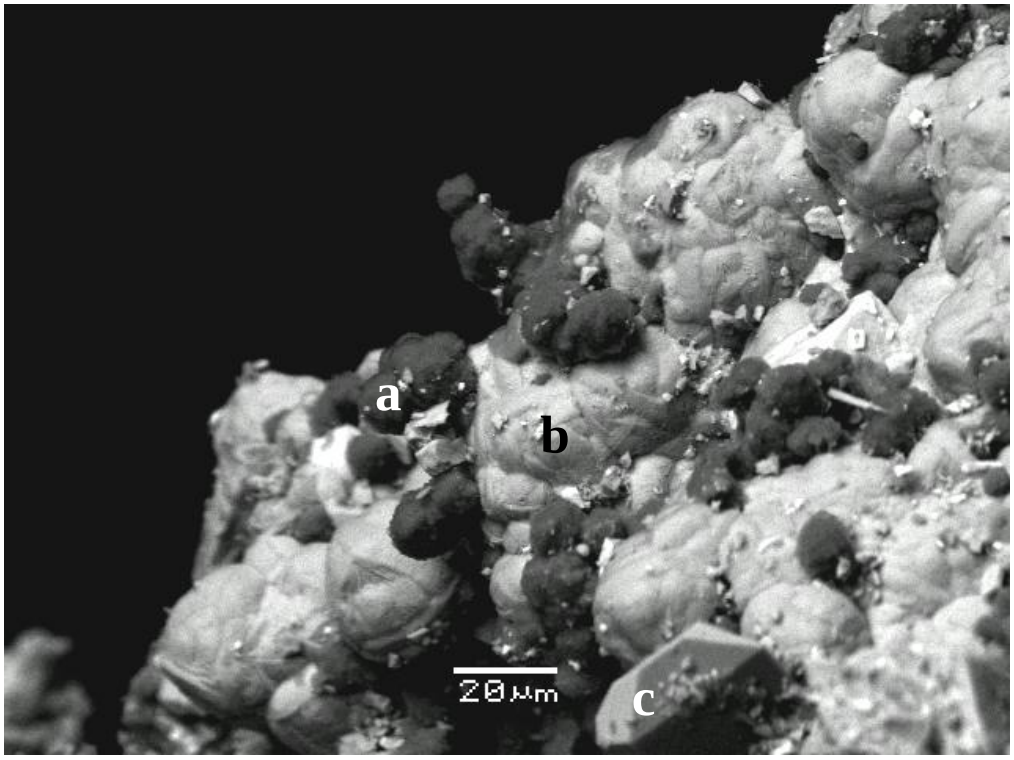

Supplementary Figure 3| SEMimage of phases lining open conduits of Politeia spire. a, K-Mg-Al-silicates (dark grey features, **b,** overgrown amorphous Sb-Zn sulfide aggregates, **c,** barite crystal.

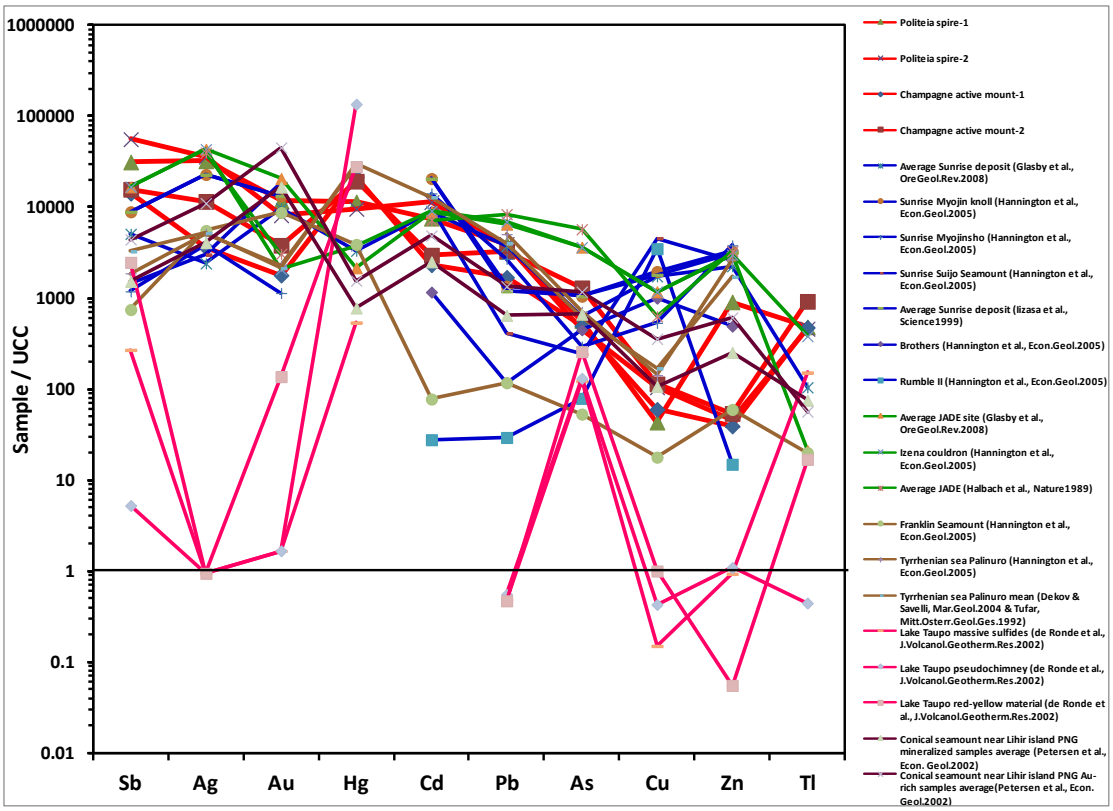

Supplementary Figure 4/ Geochemical spidergram comparing the Kolumbo vent samples with other seafloor hydrothermal deposits from various tectonic settings. Concentrations are normalized to Upper Continental Crust (UCC)[1] for selected noble (Ag, Au), potentially life-essential (Cu, Zn) and potentially toxic (Sb, Hg, Cd, As, Tl) elements. The average and maximum concentrations of Tl (510 ppm and >,1000 ppm respectively) and Sb (8,333 ppm and 2.2 wt %, respectively) are among the highest reported from modern seafloor hydrothermal systems. Average Sunrise deposit[2], Sunrise Myojin knoll[17], Sunrise Myojinsho[17], Sunrise Sujo Seamount[17], Brothers[17], Rumble II[17], Average JADE site[3], Izena cauldron [17], Average JADE[4], Franklin Seamount[17], Tyrrhenian sea Palinuro[17], Tyrrhenian sea Palinuro mean[5,6], Lake Taupo massive sulfides[7], Lake Taupo pseodochimney[7], Lake Taupo red-yellow material[7], Conical seamount-mineralized samples average[34], Conical seamount- gold-rich samples average[34]. [17] or [34]: see ref. 17, or 34, in the main article

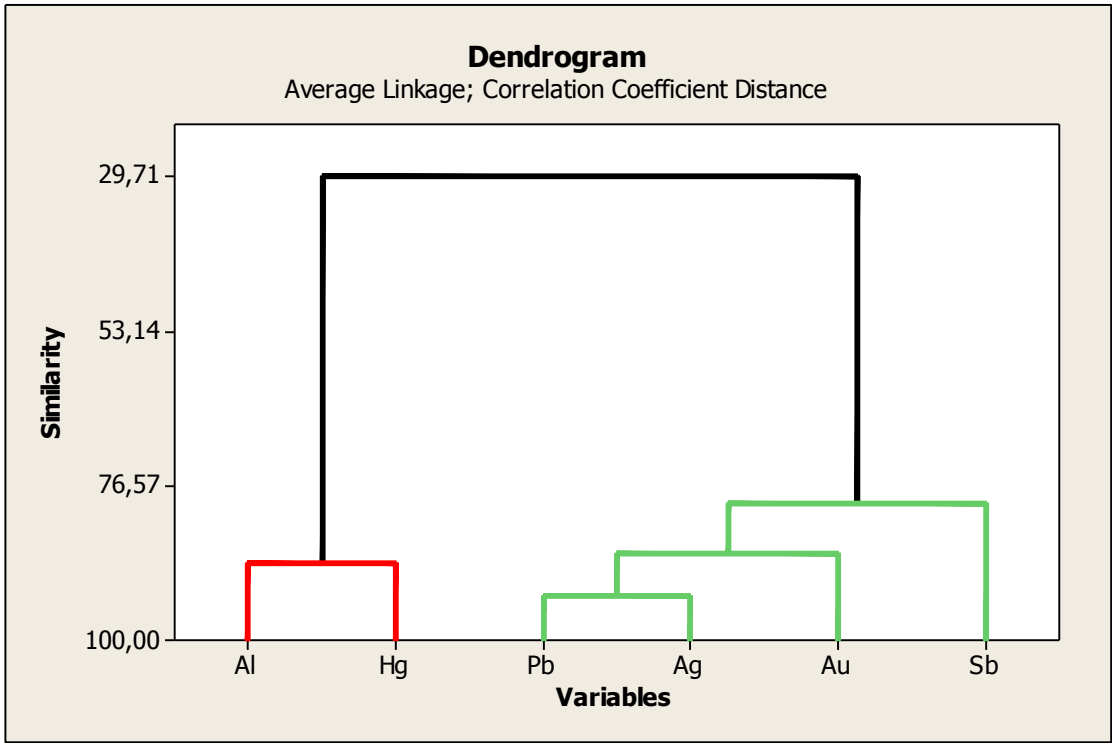

Supplementary Figure 5| Dendrogram based on statistical correlation of elements in Kolumbo samples. Variables are clustered into 2 groups according to similarity level. The first group includes Hg and Al with similarity level 88% and the second group includes Au, Pb, Ag and Sb with similarity level >79%. The relationships suggest that Au and Ag may be associated with sulfide mineral phases while Hg may be associated with aluminosilicate phases.

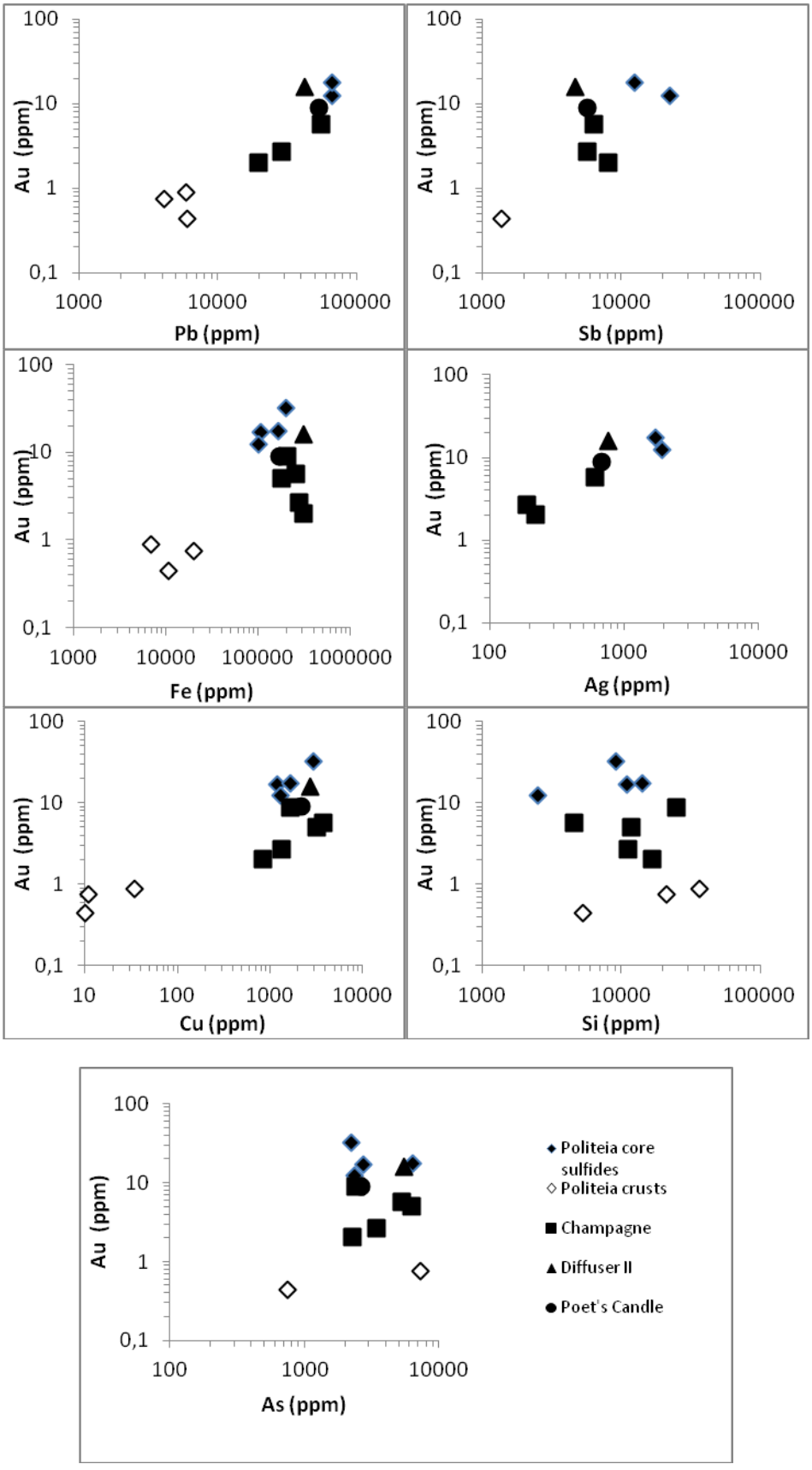

Supplementary Figure 6| Log/log plots of selected elements versus Au. Clustering of samples is observed according to vent complex, signifying different physicochemical conditions of formation. Relative enrichment of Politeia sulfides in Au, Ag, Sb and Pb is also observed.

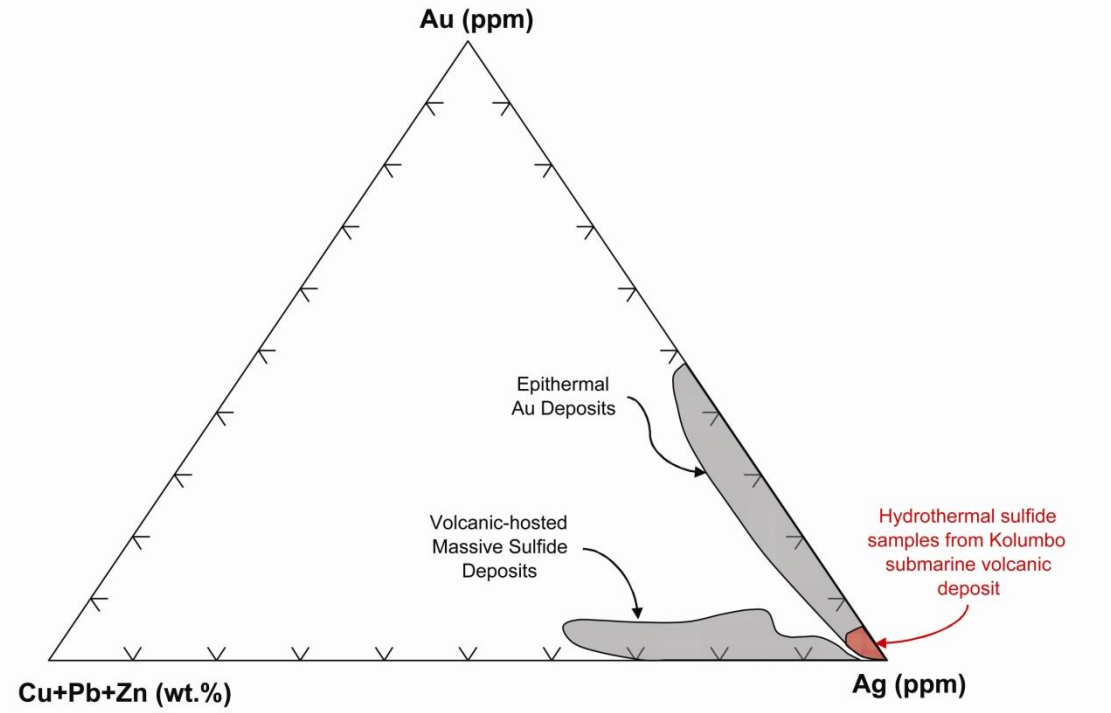

Supplementary Figure 7| Comparison of average Au, Ag and base-metal (Cu+Pb +Zn) content of samples from Kolumbo hydrothermal field and other sea-floor sulfides deposits. Compositional fields of typical epithermal gold deposits and volcanogenic massive sulfides are also shown (see Ref. 35).

Supplementary Table S1

Average content in ppm (mg kg^{-1}) of selected elements in samples from Kolumbo compared with other modern seafloor volcanogenic massive sulfide-style and epithermal-style hydrothermal deposits. Ref. XX: see reference XX in the main article.

	n	Si	Al	Fe	Pb	Sr	As	Sb	Bi	Zn	Cu	Cd	Hg	Tl	Ag	Au	Refs
Average Kolumbo deposit	14	14100	5890	166000	35000	10400	3810	8330	0.05	10200	1640	276	397	389	871	9	This study
Mid-ocean ridges:																	
S. Explorer Ridge	51	44409		252000	1000		575	42	2.0	54000	32000	200	11	43	125	0.72	Ref. 17
Endeavour Segment Main Field	83	42539		301000	5000		356	42	0.2	64000	27000	250	8	28	267	0.11	Ref. 17
Cleft segment, South cleft	16	16361		186000	1000		360	18	0.1	309000	11000	615	2	23	230	0.11	Ref. 17
East Pacific Rise																	
11N, EPR	18	12621		205000	1000		330	26	0.3	266000	16000	885	2	19	37	0.15	Ref. 17
Galapagos rift	128	118267		283000	500		120	10	1.1	35000	45000	140	4	12	37	0.29	Ref. 17
Mid-Atlantic Ridge TAG, surface and core	310	50953		272000	500		55	28	9.0	65000	49000	232	9	13	92	1.8	Ref. 17
Volcanic arcs:																	
Average Sunrise deposit	12	89753	3705	116808	63700	1704	3050	2037	10.2	150800	48700	808	166	94	128	14.6	2
Sunrise Myojin knoll	37	40669		105000	23000		5045	3565		219000	55000	1860			1215	20	Ref. 17
Average Sunrise deposit	37	40576		100480	20270		5044	3564		210890	50540	1858			1213	20	2
Suiyo seamount	13			150000	0.7		1168	585			128000				162	27.7	Ref. 39
Brothers	9			74000	2000		2155			33000	28000	105					Ref. 17
Rumble II	1			125000	500		380			1000	98000	2.5					Ref. 17
Conical seamount	40			83000	10000		3200	612		17000	3000		39		216	25	Ref. 34
Lake Taupo massive sulphides	1			253000	8.2		588	108		62.5	4.2		27	137	<0.1	<0.005	7
Back arc rifts:																	
Average JADE site		19634	3175	62251	110800	1592	17500	6710	35.6	200200	33000	794	108	19	2300	31	3
Izena couldron	40	47214		62000	118000		17500	6710	25.0	202000	33000	820	190	345	2305	3	Ref. 17
Back arc basins:																	
Tyrrhenian Sea Panarea	5	118735		105000	28000		505			62000	500	255			11		Ref. 17
Tyrrhenian Sea Palinuro	15			151000	86000		3400	750		179000	4000		1400		270	3.4	Ref. 17
Manus Basin (intraoceanic)	26			149000	1.7		11000	1130		269000	109000		17		230	15	Ref. 17

Supplementary Table S2

Average content in ppm (mg kg^{-1}) or otherwise mentioned units of selected elements in hydrothermal vent samples from the Kolumbo deposit

Sample	Sr	V	Cr	Ni	Cd	% TOC	% TOT/S
NA014-003 Politeia spire-1 (ISSC)	10900	12	55	<20	682		24
NA014-003 Politeia spire-1 (OAsL)	21700	12		55	26		
NA014-003 Politeia spire-1 (SFeC)	35200	30	123	<20	7		13
NA014-003 Politeia spire-1 composite	1030	<10	4	7	629	5.82	
NA014-005 Diffuser II	1610	<10	6	2	50	5.71	
NA014-007 Champagne active mount (base)	1180	10	5	4	44	5.77	
NA014-016 Poet's Candle sulfide	1160	<10	4	15	210	3.86	
NA014-027 Champagne active mount-1 (N=2)	11400	<8	5	38	126	5.91	30
NA014-028 Champagne active mount -2 (N=2)	11900	<8	6	5	226	5.86	30
NA014-039 Politeia spire-2 (ISSC)	4570	15	27	<20	1025		34
NA014-039 Politeia spire-2 (SFeC)	41300	43	21	<20	4		12
NA014-039 Politeia spire-2 composite	1010	<10	4	7	489	4.14	
AVERAGE	**10400**	**20**	**24**	**20**	**276**	**5.30**	**24**
MAX	**41300**	**43**	**123**	**55**	**1025**	**5.91**	**34**
N	**14**	**6**	**11**	**10**	**14**	**7**	**6**

Supplementary Table S3

Microbial taxonomy of the produced sequences for the four samples by using the RDP classifier of the Ribsomal Database Project. The most abundant observed species (OTUs) were further compared to GenBank entries using BLAST (Basic Local Alignment Search Tool, National Center for Biotechnology Information, Bethesda, MD, USA) in order to confirm their phylogenetic affiliation. The most abundant OTU closely affiliated to *Nitrosopumilus maritimus* SCM1 (99% sequence similarity) is presented in grey background.

NA014_003	NA014_007	NA014_016	NA014_042	Consensus Lineage
39	27	27	90	Archaea unclassified
615	***91***	***347***	***198***	***Thaumarchaeota;Nitrosopumilales;Nitrosopumilaceae;Nitrosopumilus***
0	0	23	81	Crenarchaeota;Thermoprotei
0	0	0	3	Crenarchaeota;Thermoprotei;Thermoproteales;Thermofilaceae;Thermofilum
9	3	5	23	Euryarchaeota
0	0	0	1	Euryarchaeota;Methanomicrobia
2	0	4	5	Euryarchaeota;Thermoplasmata;Thermoplasmatales
1096	1573	550	1333	Bacteria;unclassified
0	1	16	21	Acidobacteria
1	3	10	2	Acidobacteria;Acidobacteria_Gp10;Gp10
0	0	0	1	Acidobacteria;Acidobacteria_Gp2;Gp2
0	3	18	13	Acidobacteria;Acidobacteria_Gp21;Gp21
2	5	11	7	Acidobacteria;Acidobacteria_Gp22;Gp22
1	10	0	0	Acidobacteria;Acidobacteria_Gp23;Gp23
0	1	1	2	Acidobacteria;Acidobacteria_Gp26;Gp26
0	1	13	12	Acidobacteria;Acidobacteria_Gp6;Gp6
0	0	1	4	Acidobacteria;Acidobacteria_Gp9;Gp9
0	0	0	1	Acidobacteria;Holophagae
1	0	3	14	Actinobacteria
0	0	1	0	Actinobacteria;Acidimicrobiales
0	0	0	1	Actinobacteria;Acidimicrobiales;Iamiaceae;Iamia
0	0	1	0	Actinobacteria;Actinomycetales;Brevibacteriaceae;Brevibacterium
0	1	5	1	Actinobacteria;Actinomycetales;Corynebacteriaceae;Corynebacterium
0	2	0	0	Actinobacteria;Actinomycetales;Geodermatophilaceae
0	1	1	0	Actinobacteria;Actinomycetales;Micrococcaceae;Micrococcus
0	0	1	0	Actinobacteria;Actinomycetales;Nocardioidaceae;Nocardioides
0	4	8	6	Actinobacteria;Actinomycetales;Propionibacteriaceae;Propionibacterium
174	72	20	9	Bacteroidetes
1	10	1	0	Bacteroidetes;Bacteroidetes_incertae_sedis;Fulvivirga
0	0	1	0	Bacteroidetes;Bacteroidia;Bacteroidales;Prevotellaceae;Prevotella
7	3	0	0	Bacteroidetes;Flavobacteria;Flavobacteriales
1	1	5	0	Bacteroidetes;Flavobacteria;Flavobacteriales;Cryomorphaceae
78	8	166	1	Bacteroidetes;Flavobacteria;Flavobacteriales;Flavobacteriaceae
1	0	0	0	Bacteroidetes;Flavobacteria;Flavobacteriales;Flavobacteriaceae;Elizabethkingia
0	2	3	0	Bacteroidetes;Flavobacteria;Flavobacteriales;Flavobacteriaceae;Gaetbulibacter
0	0	1	0	Bacteroidetes;Flavobacteria;Flavobacteriales;Flavobacteriaceae;Lacinutrix
1	0	10	0	Bacteroidetes;Flavobacteria;Flavobacteriales;Flavobacteriaceae;Lutimonas
1	3	1	0	Bacteroidetes;Flavobacteria;Flavobacteriales;Flavobacteriaceae;Muricauda
13	16	9	2	Bacteroidetes;Sphingobacteria;Sphingobacteriales
0	0	0	1	Bacteroidetes;Sphingobacteria;Sphingobacteriales;Chitinophagaceae
4	9	5	0	Bacteroidetes;Sphingobacteria;Sphingobacteriales;Rhodothermaceae
1	1	0	0	Bacteroidetes;Sphingobacteria;Sphingobacteriales;Rhodothermaceae;Rhodothermus
4	1	5	0	Bacteroidetes;Sphingobacteria;Sphingobacteriales;Saprospiraceae
0	0	1	1	BRC1;BRC1_genera_incertae_sedis
1	0	0	0	Caldiserica;Caldisericia;Caldisericales;Caldisericaceae;Caldisericum

6	1	3	17	Chlamydiae;Chlamydiae;Chlamydiales
0	0	0	3	Chlamydiae;Chlamydiae;Chlamydiales;Parachlamydiaceae
0	8	0	1	Chlamydiae;Chlamydiae;Chlamydiales;Parachlamydiaceae;Parachlamydia
0	11	0	0	Chlamydiae;Chlamydiae;Chlamydiales;Simkaniaceae;Simkania
0	1	1	1	Chlamydiae;Chlamydiae;Chlamydiales;Waddliaceae;Waddlia
0	2	0	12	Chloroflexi
0	26	0	6	Chloroflexi;Anaerolineae;Anaerolineales;Anaerolineaceae
0	0	0	1	Chloroflexi;Caldilineae;Caldilineales;Caldilineaceae;Caldilinea
0	0	0	12	Chloroflexi;Dehalococcoidetes
0	0	0	6	Chloroflexi;Dehalococcoidetes;Dehalogenimonas
0	0	0	1	Cyanobacteria;Cyanobacteria;Family II;GpIIa
0	1	2	1	Deinococcus-Thermus;Deinococci;Deinococcales;Trueperaceae;Truepera
1	0	0	0	Deinococcus-Thermus;Deinococci;Thermales;Thermaceae;Oceanithermus
0	0	0	4	Firmicutes
0	0	0	1	Firmicutes;Bacilli;Bacillales;Bacillaceae;Bacillus
0	0	1	0	Firmicutes;Bacilli;Bacillales;Staphylococcaceae;Gemella
0	0	1	0	Firmicutes;Bacilli;Bacillales;Staphylococcaceae;Staphylococcus
0	0	1	0	Firmicutes;Bacilli;Lactobacillales
1	2	1	1	Firmicutes;Bacilli;Lactobacillales;Lactobacillaceae;Lactobacillus
0	1	9	3	Firmicutes;Bacilli;Lactobacillales;Streptococcaceae;Streptococcus
0	0	2	0	Firmicutes;Clostridia;Clostridiales;Incertae Sedis XI;Finegoldia
0	1	0	0	Firmicutes;Clostridia;Clostridiales;Peptococcaceae
0	0	1	0	Firmicutes;Clostridia;Clostridiales;Ruminococcaceae;Faecalibacterium
0	0	1	1	Firmicutes;Clostridia;Clostridiales;Veillonellaceae
1	1	0	0	Firmicutes;Clostridia;Clostridiales;Veillonellaceae;Veillonella
0	0	1	0	Lentisphaerae;Lentisphaeria;Lentisphaerales;Lentisphaeraceae;Lentisphaera
66	0	0	0	Nitrospira;Nitrospira;Nitrospirales;Nitrospiraceae
0	5	8	0	Nitrospira;Nitrospira;Nitrospirales;Nitrospiraceae;Nitrospira
68	15	0	0	OD1;OD1_genera_incertae_sedis
155	281	79	106	Planctomycetes;Planctomycetacia;Planctomycetales;Planctomycetaceae
3	31	9	5	Planctomycetes;Planctomycetacia;Planctomycetales;Planctomycetaceae;Blastopirellula
0	0	1	0	Planctomycetes;Planctomycetacia;Planctomycetales;Planctomycetaceae;Pirellula
25	17	5	0	Planctomycetes;Planctomycetacia;Planctomycetales;Planctomycetaceae;Planctomyces
2	1	2	1	Planctomycetes;Planctomycetacia;Planctomycetales;Planctomycetaceae;Rhodopirellula
206	58	85	33	Proteobacteria
197	101	138	16	Alphaproteobacteria
34	19	33	0	Alphaproteobacteria;Caulobacterales;Hyphomonadaceae
1	0	0	0	Alphaproteobacteria;Caulobacterales;Hyphomonadaceae;Maricaulis
5	2	6	0	Alphaproteobacteria;Parvularculales;Parvularculaceae;Parvularcula
3	0	17	1	Alphaproteobacteria;Rhizobiales
0	0	0	4	Alphaproteobacteria;Rhizobiales;Bradyrhizobiaceae
0	0	1	0	Alphaproteobacteria;Rhizobiales;Bradyrhizobiaceae;Afipia
0	0	1	1	Alphaproteobacteria;Rhizobiales;Hyphomicrobiaceae
1	0	2	0	Alphaproteobacteria;Rhizobiales;Hyphomicrobiaceae;Filomicrobium
1	0	2	0	Alphaproteobacteria;Rhizobiales;Phyllobacteriaceae
0	0	0	2	Alphaproteobacteria;Rhizobiales;Rhizobiaceae;Rhizobium
42	13	33	1	Alphaproteobacteria;Rhodobacterales;Rhodobacteraceae
1	6	0	0	Alphaproteobacteria;Rhodobacterales;Rhodobacteraceae;Lutimaribacter
0	0	0	1	Alphaproteobacteria;Rhodobacterales;Rhodobacteraceae;Paracoccus
0	0	5	0	Alphaproteobacteria;Rhodobacterales;Rhodobacteraceae;Roseovarius
0	41	0	1	Alphaproteobacteria;Rhodospirillales
12	20	62	9	Alphaproteobacteria;Rhodospirillales;Rhodospirillaceae
0	0	2	0	Alphaproteobacteria;Rhodospirillales;Rhodospirillaceae;Thalassobaculum
2	0	0	0	Alphaproteobacteria;Rickettsiales;SAR11;Pelagibacter
0	7	1	0	Alphaproteobacteria;Sphingomonadales;Sphingomonadaceae;Sphingomonas
36	0	3	0	Betaproteobacteria
0	1	0	0	Betaproteobacteria;Burkholderiales;Burkholderiaceae;Burkholderia
0	0	0	2	Betaproteobacteria;Burkholderiales;Burkholderiales_incertae_sedis;Aquabacterium

0	1	0	0	Betaproteobacteria;Burkholderiales;Comamonadaceae;Pelomonas
0	0	1	0	Betaproteobacteria;Neisseriales;Neisseriaceae
0	1	0	0	Betaproteobacteria;Nitrosomonadales;Nitrosomonadaceae
0	1	1	0	Betaproteobacteria;Rhodocyclales;Rhodocyclaceae
8	59	16	21	Deltaproteobacteria
4	0	0	0	Deltaproteobacteria;Bdellovibrionales;Bacteriovoracaceae;Bacteriovorax
24	6	0	16	Deltaproteobacteria;Desulfobacterales;Desulfobacteraceae
0	1	0	0	Deltaproteobacteria;Desulfobacterales;Desulfobacteraceae;Desulfatiferula
5	31	0	0	Deltaproteobacteria;Desulfobacterales;Desulfobulbaceae
0	0	2	0	Deltaproteobacteria;Desulfuromonadales
0	0	1	0	Deltaproteobacteria;Desulfuromonadales;Geobacteraceae
2	1	2	1	Deltaproteobacteria;Myxococcales
0	2	0	0	Deltaproteobacteria;Myxococcales;Haliangiaceae;Haliangium
1	1	1	0	Deltaproteobacteria;Myxococcales;Nannocystaceae
0	0	6	0	Epsilonproteobacteria;Campylobacterales
32	1	0	0	Epsilonproteobacteria;Campylobacterales;Campylobacteraceae
4	0	0	0	Epsilonproteobacteria;Campylobacterales;Campylobacteraceae;Sulfurospirillum
17	1	3	0	Epsilonproteobacteria;Campylobacterales;Helicobacteraceae
98	1	5	0	Epsilonproteobacteria;Campylobacterales;Helicobacteraceae;Sulfurimonas
1	0	0	0	Epsilonproteobacteria;Campylobacterales;Helicobacteraceae;Wolinella
626	369	332	35	Gammaproteobacteria
2	1	0	0	Gammaproteobacteria;Alteromonadales
3	3	0	1	Gammaproteobacteria;Chromatiales
23	0	7	0	Gammaproteobacteria;Chromatiales;Ectothiorhodospiraceae
0	3	0	2	Gammaproteobacteria;Enterobacteriales;Enterobacteriaceae
0	2	1	0	Gammaproteobacteria;Enterobacteriales;Enterobacteriaceae;Escherichia/Shigella
0	5	0	0	Gammaproteobacteria;Gammaproteobacteria_incertae_sedis
1	2	0	1	Gammaproteobacteria;Gammaproteobacteria_incertae_sedis;Sedimenticola
1	0	0	0	Gammaproteobacteria;Legionellales;Legionellaceae
0	0	10	0	Gammaproteobacteria;Methylococcales;Methylococcaceae
32	0	5	0	Gammaproteobacteria;Methylococcales;Methylococcaceae;Methylomonas
0	0	4	3	Gammaproteobacteria;Pasteurellales;Pasteurellaceae
0	1	0	0	Gammaproteobacteria;Pseudomonadales;Moraxellaceae
0	1	9	0	Gammaproteobacteria;Pseudomonadales;Moraxellaceae;Acinetobacter
0	0	1	0	Gammaproteobacteria;Pseudomonadales;Moraxellaceae;Psychrobacter
2	19	186	22	Gammaproteobacteria;Pseudomonadales;Pseudomonadaceae;Pseudomonas
8	0	0	0	Gammaproteobacteria;Thiotrichales;Piscirickettsiaceae;Thiomicrospira
0	1	0	1	Gammaproteobacteria;Xanthomonadales;Xanthomonadaceae;Stenotrophomonas
16	0	0	2	Spirochaetes;Spirochaetes;Spirochaetales;Spirochaetaceae;Spirochaeta
1	3	2	3	TM7;TM7_genera_incertae_sedis
3	1	0	0	Verrucomicrobia
5	1	0	2	Verrucomicrobia;Opitutae
1	0	0	0	Verrucomicrobia;Opitutae;Opitutales;Opitutaceae
1	0	0	0	Verrucomicrobia;Opitutae;Puniceicoccales;Puniceicoccaceae
5	11	2	0	Verrucomicrobia;Verrucomicrobiae;Verrucomicrobiales;Verrucomicrobiaceae
0	1	0	0	WS3;WS3_genera_incertae_sedis
33	14	4	24	Unclassified

Supplementary Table S4

Bray-Curtis similarities of microbial community composition among the four investigated samples at an OTU (observed species) level and phylum level.

	NA014_003	**NA014_007**	**NA014_016**
	OTU level		
NA014_007	0		
NA014_016	25.53	0	
NA014_042	0	7.15	0
	Phylum level		
NA014_007	66.25		
NA014_016	82.06	60.03	
NA014_042	52.47	72.12	50.44

Supplementary References

1. Rudnick, R. & Gao, S. Composition of the continental crust. In "The Crust", Holland, H.D. & Turekian, K.K. eds. Treatise on Geochemistry. *Elsevier* Pergamon, Oxford **3**, 1-64 (2003).
2. Iizasa, K. *et al*. A Kuroko-Type polymetallic sulfide deposit in a submarine silicic caldera. *Science* **283**, 975-977 (1999).
3. Glasby, G. P., Iizasa, K., Hannington, M., Kubota, H. , Notsu, K. Mineralogy and composition of Kuroko deposits from northeastern Honshu and their possible modern analogues from the Izu-Ogasawara (Bonin) Arc south of Japan: Implications for mode of formation. *Ore Geology Reviews* **34**, 247-560 (2008).
4. Halbach, P., *et al*. Probable modern analogue of Kuroko-type massive sulfide deposits in the Okinawa Trough back-arc basin. *Nature* **338**, 496-499 (1989).

5. Dekov, V.M., Savelli, C. Hydrothermal activity in the SE Tyrrhenian Sea: an overview of 30 years of research. *Mar. Geol.* **204**, 161–185 (2004).
6. Tufar, W. Paragenesis of complex massive sulfide ores from the Tyrrhenian Sea. *Mitteilungen der Österreichischen Geologischen Gesellschaft* **84**, 265–300 (1991).
7. de Ronde, C.E.J. *et al*. Discovery of active hydrothermal venting in Lake Taupo, New Zealand. *Journal of Volcanology and Geothermal Research* **115**, 257-275 (2002).